Diploma thesis

Radiological-anatomical distribution patterns of Jakob-Creutzfeldt disease in relation to cortical systems

Involvement of the cortex with regard to phylogenesis

submitted by

Felix Gunzer

to gain the academic degree

Doktor der gesamten Heilkunde

(Dr. med. univ.)

at the

Medical University of Graz

conducted at the

Department of Radiology

Division of Neuroradiology, Vascular and Interventional Radiology

supervised by

Ao.Univ.-Prof. Dipl.-Ing. Dr.med.univ. Josef Simbrunner

Dr. med. univ. Eva Maria Hassler

Graz, 01.03.2021

Eidesstattliche Erklärung

Ich erkläre ehrenwörtlich, dass ich die vorliegende Arbeit selbstständig und ohne fremde Hilfe verfasst habe, andere als die angegebenen Quellen nicht verwendet habe und die den benutzten Quellen wörtlich oder inhaltlich entnommenen Stellen als solche kenntlich gemacht habe.

Graz, am 01. März 2021 *Felix Gunzer eh*

Preface

»Shall we do it?« »Well, then let's go, we shall do it!«

Otto Stern and Walther Gerlach

The moment that would set the course for MRI.

Acknowledgement

I wish to show my appreciation to my advisors Prof. Josef Simbrunner and Dr Eva Maria Hassler, for the continuous support of this diploma thesis, for their patience, knowledge and warm-heartedness.

I want to express my sincere gratitude to Dr Gernot Reishofer and Fritz Studencnik for their help and guidance. Without them, this thesis would never have been possible.

And of course, I want to thank my parents. This work is one of the many results I owe you. Your love, caring, and sacrifices for my brothers and me are virtues I will always be grateful to.

Table of contents

List of abbreviations

AAL	Automated anatomical labelling (atlas)
ADC	Apparent diffusion coefficient map
AF	Arcuate fasciculus
CB	Cingulate bundle
CCF	Connectome Coordination Facility
CSF	Cerebrospinal fluid
CT	Computer tomography
dJCD	Dura mater graft-associated Jakob-Creutzfeldt disease
DWI	Diffusion-weighted imaging
EDC	Exponential diffusion coefficient map
EEG	Electroencephalography, Electroencephalogram
fCJD	Familial Creutzfeldt-Jakob disease
FFI	Fatal familial insomnia
FLAIR	Fluid-attenuated inversion recovery
FOF	Fronto-occipital fasciculus
gJCD	Genetic (familial) Jakob-Creutzfeldt disease
GPI	Glycosyl phosphatidylinositol
GSS	Gerstmann-Sträussler-Scheinker syndrome
HCP	Human Connectome Project
hGH JCD	Human pituitary-derived growth hormone-associated Jakob-Creutzfeldt disease
ICDM-152	Standardised brain template in MNI space
IFO	Inferior fronto-occipital fasciculus
iJCD	Iatrogenic Jakob-Creutzfeldt disease
ILF	Inferior longitudinal fasciculus
IQ-QuIC	Improved real-time quaking-induced conversion
JCD	Jakob-Creutzfeldt disease
MdLF	Middle longitudinal fasciculus
MM	Multimodal cortex
MNI	Montreal Neurological Institute
MRI	Magnetic resonance imaging
ND	Not definable areas
PF	Prefrontal cortex
PL	Paralimbic cortex
PRNP	Human prion protein gene
PrP	Prion protein
PrP^{TSE}	Abnormal prion protein

PSWC	Periodical sharp wave complex
RSNA	Radiological Society of North America
RT-QuIC	Real-time quaking-induced conversion
sJCD	Sporadic Jakob-Creutzfeldt disease
SLF	Superior longitudinal fasciculus
SMA	Supplementary motor cortex
SPM12	Statistical Parametric Mapping software
TE	Echo time
TR	Relaxation time
TSE	Transmissible spongiform encephalopathies
UF	Uncinate fasciculus
vJCD	Variant Jakob-Creutzfeldt disease

List of Figures

List of Tables

Zusammenfassung

Prionenkrankheiten sind eine Gruppe von Erkrankungen, die sowohl Menschen als auch Tiere betreffen, in der Regel mit schnell fortschreitender Symptomatik auftreten und immer tödlich enden. Erkrankungen ausgelöst durch Prionen treten sehr selten auf, werden aber derzeit so häufig wie nie gemeldet. Das Ziel dieser Arbeit ist die Untersuchung der radiologischen Verteilungsmuster kortikaler Läsionen im MRT in PatientInnen, die an Jakob-Creutzfeldt erkrankten. Diese Verteilungsmuster werden in Bezug zu funktionellen kortikalen Systemen anhand des „dual-origin concept“ und der Phylogenese des Kortex gestellt und untersucht. Dies soll zu einem besseren Verständnis der Erkrankung Jakob-Creutzfeldt und der Bildung neuer Hypothesen dienen.

Es wurden zehn PatientInnen mit der Diagnose Jakob-Creutzfeldt retrospektiv selektiert und die dazugehörigen MRT Bilder extrahiert. Die MRT Aufnahmen wurden mittels SPM12 normalisiert und im MNI Raum registriert. Hirnläsionen wurden segmentiert und daraufhin mit einem selbstgeschriebenen Programmcode neuroanatomischen Arealen automatisch zugeordnet. Der Talairach Atlas und der AAL Atlas wurden für die Zuordnung der jeweiligen MRT Voxel verwendet sowie zur späteren statistischen Analyse herangezogen.

Als Ergebnisse konnten Hypothesen zum axonalen Transport von Prionen, zum Zusammenhang zwischen klinischer Symptomatik und funktioneller kortikaler Systeme sowie zur Involvierung hauptsächlich neokortikaler Strukturen gefestigt werden. Die Annahme, dass Jakob-Creutzfeldt den primär motorischen Kortex ausspare, sollte aufgrund der Ergebnisse dieser Arbeit überdacht werden.

Abstract

Prion diseases are a group of diseases that affect humans and animals, usually present with rapidly progressive symptoms and are always fatal. Diseases triggered by prions occur very rarely but are currently reported more frequently than ever. This study investigates the radiological distribution patterns of cortical lesions on MRI in patients with Jakob-Creutzfeldt disease. These distribution patterns will be related to functional cortical systems based on the *dual-origin* concept and the cortex's phylogenesis. This should lead to a better understanding of Jakob-Creutzfeldt disease and the formation of new hypotheses.

Ten patients with the diagnosis Jakob-Creutzfeldt were retrospectively selected, and the corresponding MRI images were extracted. The MRI scans were normalised using SPM12 and registered in MNI space. The brain lesions were segmented and then automatically assigned to neuroanatomical areas using a self-written program code. The Talairach atlas and the AAL atlas were used to assign the respective MRI voxels and were taken into account in following statistical analyses.

As results, hypotheses on the axonal transport of prions, the connection between clinical symptoms and functional cortical systems, and the involvement of mainly neocortical structures could be consolidated. The assumption that Jakob-Creutzfeldt spares the primary motor cortex should be reconsidered based on this thesis' results.

Introduction

Prion diseases are a group of disorders affecting both humans and animals, usually occurring with rapidly progressive symptomatic and always ending fatally. Prion diseases appear seemingly rarely but are now reported more often than ever (1). *Jakob-Creutzfeldt disease* (JCD), especially the sporadic variant (sJCD), represents the most common prionic disease being responsible for approximately 85% of the reported cases around the world (2). Hence, a precise and early diagnosis of JCD is crucial for patients and their relatives. Furthermore, strict surveillance is mandatory to prevent iatrogenic cases of JCD. One essential tool to support clinicians and particularly radiologists in uncovering such rare cases is the magnetic resonance imaging technology (MRI). Nonetheless, a definitive diagnose of JCD can only be made via biopsy of brain tissue post-mortem (3–7). Therefore, it is even more critical to assess radiologic patterns of distribution of JCD in order to have a better understanding of the disease as well as to determine the reliability of MRI for clinical diagnosis.

1.1 History of Jakob-Creutzfeldt disease

It was in 1920 when the German neuropathologist Hans Gerhard Creutzfeldt (1885–1964) published a case report of a 22-year-old woman with a rare fatal neurological disorder (8). At the same time, three cases of rapidly progressive dementia and spasticities associated with cortical, striatal, and spinal degeneration examined by the neurologist Professor Alfons Maria Jakob (1884–1931) had been read at the 10th annual meeting of the Society of German Neurologists, held in Leipzig 1920 (9). One year later, in 1921, Jakob published three papers, "Über eigenartige Erkrankungen des Zentralnervensystems mit bemerkenswerten anatomischen Befunden" (10–12). In these papers and one additional article from 1923, he reported five cases of unusual neurologic disorders (13).

In his second paper, Jakob reports that Creutzfeldt's case may have also described this new disease, referring to a "nosologically very closely connected if not identical affection" ("nosologisch sehr nahestehende, wenn nicht wesensgleiche Affektion") (11). Because of that, the term *Creutzfeldt-Jakob Krankheit* (Creutzfeldt-Jakob disease) was first used by the

German neurologist Walther Spielmeyer in 1922 (14). Creutzfeldt may have reported later that "his case did not bear any resemblance to the cases described by Jakob." (15) Today's medicine considers that the case of Creutzfeldt was erroneously assigned to the entity Jakob had described. In fact, later on, only two cases of Jakob's five cases have been confirmed to be JCD (16). Therefore, JCD or *Jakob disease* may be the more appropriate term (16,17).

For many years, the aetiology and pathogenesis of JCD remained unknown. It was not until 1968 that JCD was discovered to be transmissible (18) and related other rare neurological disorders assigned to a group nowadays called *Transmissible spongiform encephalopathies* (TSE) or *human prion diseases*. Historically, three clinicopathological phenotypes were allocated to human prion diseases: familial CJD (fCJD), Gerstmann-Sträussler-Scheinker syndrome (GSS), and Fatal familial insomnia (FFI). GSS and FFI are considered until today. However, some genetic prion diseases do not fit into this categorisation anymore (19).

In the 20th century, the scientific community recognised JCD as a distinct entity early on, but it lacked applicable diagnostic criteria (20). It was not until a comprehensive evaluation of cerebral grey matter that showed characteristic spongiform changes in patients with JCD leading to the term *subacute spongiform encephalopathy* (21). Hence, the first significant pathologic patterns had been determined. However, the cause for JCD remained unproven, although some scientists (22,23) already suspected some small agents with different capabilities being more resistant to external stress than viruses or bacteria. Prusiner (24,25) was the first who formulated the prion hypothesis, which states that small transmissible particles composed of modified host cell surface glycoprotein accumulate in brains affected by JCD or related disorders. He called those *proteinaceous infectious particles* or *prion proteins* (PrP) for short (25). His research was awarded the 1977 Nobel Prize in Medicine.

Decades later, modern cell biology and molecular genetics still support this hypothesis (3–7). Nevertheless, it was not until discovering the *human prion protein* gene, PRNP, that led to the classification of genetic prion diseases (7). PRNP is located on the short arm of chromosome 20, containing 253 amino acids. Autosomal-dominant mutations in this gene

are associated with genetic prion diseases (7). These genetic forms of TSE are also experimentally transmissible, thereby supporting the prion hypothesis (3,4).

Nowadays, this theorem is still supported and has been implemented in new classifications, clinical algorithms, and radiologic imaging.

1.2 Classification of Prion Diseases

In the 5th century BCE, Hippocrates might have described TSEs in cattle and goats (26), but one of the first diseases allocated to TSEs was *Kuru.* Gajdusek et al. (27) discovered that this disease was associated with endocannibalism in the Fore tribe in Papua, New Guinea, being transmitted from deceased ancestors to their living relatives (28). However, after the interruption of this ritual, kuru became almost extinct. They also reported that they had transmitted kuru to primates in 1966 (27), two years before the same transmissibility was discovered for JCD. This discovery earned Gajdusek the 1976 Nobel Prize in Medicine. It was also found that TSEs not only affect humans but animals, such as sheep and goats (scrapie) or cattle (bovine spongiform encephalopathy) (7).

In general, human prion diseases can be classified as idiopathic, genetic, and acquired (see Table 1). Human prion diseases of unknown aetiology, including sporadic JCD (sJCD), sporadic fatal insomnia, and variably protease-sensitive prionopathy, account for 85% to

Table 1 **TSE subtypes**

Variables	Subtypes
Sporadic (85-90%)	Sporadic JCD (sJCD)
	Sporadic fatal insomnia
	Variably protease-sensitive prionopathy
Genetic (10-15%)	Genetic (familial) JCD (gJCD)
	Fatal familial insomnia (FFI)
	Gerstmann-Sträussler-Scheinker disease (GSS)
Acquired (<1%)	Iatrogenic JCD (iJCD)
	Kuru
	Variant JCD (vJCD)

Source: (2:p.2)

90% of all cases in the world (29). These are followed by prion diseases being of hereditary origin represented by genetic (familial) JCD (gJCD), FFI, and GSS. Acquired human TSEs are considered extremely rare and account for less than 1% of all cases worldwide (19,30,31).

1.2.1 Types of JCD

JCD is just one entity of human prion diseases or TSE and occurs sporadically, genetically, or acquired. Four forms are described: sporadic JCD, genetic (familial) JCD, iatrogenic JCD, and variant JCD. Although all variants are inevitably lethal, their pathomechanisms are very different.

1.2.1.1 Variant JCD

The variant form of JCD is the last subgroup added to the classification of human prion diseases. The first cases of vJCD were described in the United Kingdom in 1996 (32,33) when two unusually young patients suffering from JCD with no specific risk factors for the other three subgroups. It was then discovered and already suspected that contaminated beef products from BSE-affected cattle can infect humans and that BSE and vJCD are caused by the same strain of prions (34). Also, cases were reported where transmission occurred via blood transfusion (34–36). As a consequence, people with risk factors, probable or possible JCD are not permitted to donate blood.

1.2.1.2 Iatrogenic JCD

Iatrogenic JCD belongs to the same group as vJCD due to the transmission of prions but through contaminated surgical and medical equipment. Clinically, iJCD is subdivided into two types: *Dura mater graft-associated JCD* (dJCD), transmitted via cadaveric dura grafts, and *Human pituitary-derived growth hormone-associated JCD* (hGH JCD), also transmitted through hGH grafts from contaminated cadavers (6).

1.2.1.3 Genetic JCD

Genetic JCD is associated with mutations of PRNP, transmitted autosomal-dominantly with variable penetrance (19). A plethora of different mutations are allocated to various neuropathological features. Although gJCD and sJCD underly different pathological

mechanisms, they somehow overlap. It was unexpectedly found that in some patients suffering from sporadic JCD, genetic testing also revealed mutations of PRNP, and therefore, the term genetic JCD instead of familial prion disease is recommended (37). Furthermore, naturally occurring polymorphisms in PRNP are considered to influence the susceptibility for misfolding or transmission of PrP, making it challenging to classify gJDC accurately.

1.2.1.4 Sporadic JCD

Sporadic JCD, as by far the most common group of prion diseases in the world with an annual incidence of two cases per 1 million inhabitants (3), will be the main focus of this thesis. Its aetiology remains unknown but is generally regarded as a neurodegenerative illness with spontaneous somatic mutations of PRNP or stochastic structural changes in PrP (3).

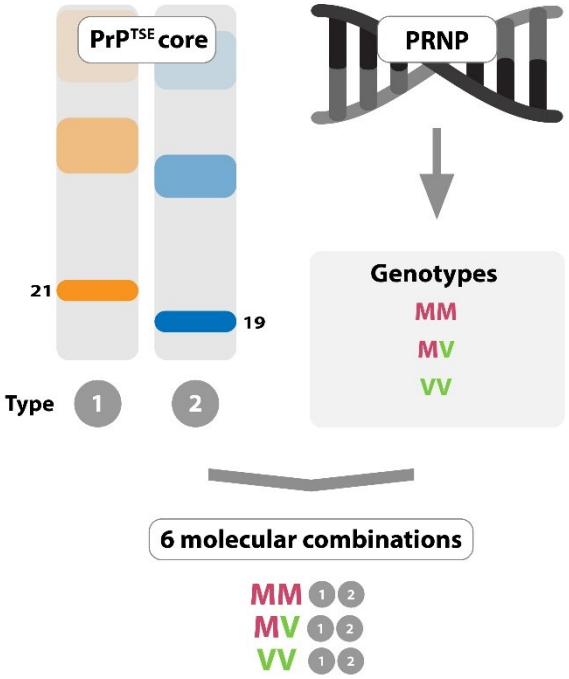

Figure 1. (3:p.5) Molecular basis of sJCD phenotypes. PrP^{TSE} types differ in their C-terminal core (21 vs 19 kDa), showing two distinct patterns in electrophoresis. Due to the naturally occurring polymorphism in the PRNP gene, three genotypes (MM, MV, VV) are possible. Both features combined result in six molecular combinations.

In the current classification of TSE, there are six phenotypical subtypes recognised (see table 2). However, some authors consider only five phenotypes distinctive for sJCD because sporadic fatal insomnia has the same molecular pattern as the thalamic form of sJCD, thus,

mimicking the disease (38–40). At the molecular level, these phenotypes correlate each with their abnormal prion protein (PrP^{TSE}) type and a specific codon 129 combination (41). PrP^{TSE} appears in two types (type 1 and 2) and combined with the polymorphic codon 129, encoding for either valine (V) or methionine (M), six molecular combinations result (MM1, MM2, VV1, VV2, MV1, MV2) (41). Nonetheless, there are three (resp. four) exceptions: First, cases of sJCD type MM1 and MV1 appear indiscernible and, thus, have been merged into one subgroup (MM/MV 1). Second, the MM2 subtype is subdivided into a cortical (MM2C) and thalamic variant (MM2T) according to the location of lesions predominantly found in both types (3). As already mentioned, MM2T is not allocated to sJCD by all authors but sporadic fatal insomnia (38–40). Finally, the MV2 subtype was identified to present either with cerebellar amyloid plaques of the kuru type, labelled MV2-kuru (MV2K) or with predominantly cortical lesions, denoted MV2-cortical (MV2C) (41). Although neuropathological examination from brain tissue is required for a definite diagnosis of sJCD (3), surveillance studies have allowed implementing clinical diagnostic criteria, which will be discussed in the next chapter.

Table 2 **Classification of genetic subtypes of sJCD**

	Subtypes				
Features	**MM/MV1**	**VV2**	**MV2K**	**MM2T/C**	**VV1**
Mean age of onset	68 (31–86)	64 (40–83)	65 (36–83)	T: 52 (26-71) C: 64 (49-77)	44 (19–55)
Duration of illness	4 (1–24)	17 (4–48)	6.5 (3–18)	16 (8–36)	21 (17–42)
Clinical signs/ symptoms	Dementia, cortical anopsia, ataxia, myoclonus	Prominent ataxia, late dementia	Ataxia, dementia, extrapyramidal symptomatic	Progressive dementia, ataxia, diplopia, psychiatric signs, sleep loss, late cognitive impairment	Dementia at onset, later ataxia and extrapyramidal symptomatic
14-3-3 status	95% positive)	80% positive	Similar to VV2	91% positive	~100%
MRI findings	70% MRI hyperintensity in basal ganglia or cortex	70% hyperintensity in basal ganglia, 45% in thalamus	79% hyperintensity in basal ganglia, + pulvinar sign	Cortical changes in 25%, rare basal ganglia involvement	Frequent cortical hyperintensity, rare basal ganglia involvement
EEG findings	PSWCs in 80%	PSWCs in 10%	Similar to VV2	PSWCs in 42%	PSWCs negative
Frequency	65%	15-20%	10%	5%	1%

Source (3:p.6,42:p.3)

1.3 Diagnostic Approach

A definite diagnosis of JCD in vivo is rarely achieved as it is only possible via extraction and pathological analysis of grey matter specimens, presenting a nonnegligible risk for the patient (7). Due to the number of TSE entities and often encountered symptomatic similarities between them, the clinical differentiation relies on the assessment of risk factors and clinical hallmarks (shown in Table 2) (30). In the following, this thesis will mainly focus on the diagnostic approach of sJCD. In 1979, the first clinical diagnostic criteria were formulated, primarily consisting of EEG patterns and symptoms (31). Later on, when radiology became much more straightforward, MRI imaging crucially supported those diagnostic criteria (2,43–47). Currently, the probable diagnosis of sJCD is made by clinical signs and results of at least one of the following tests: detection of 14-3-3 protein in cerebrospinal fluid (CSF), MRI signal abnormalities in caudate, putamen, or cortical regions either on DWI or FLAIR sequences, and detection of periodic sharp and slow wave complexes in EEG (PSWCs) (42,48,49). In the latest guidelines, neuropsychiatric disorders plus positive QuIC (quaking-induced conversion) assay in cerebrospinal fluid (CSF) or other tissues also supports the diagnosis *probable sJCD* (49). The clinical features are defined as rapidly progressive dementia plus at least two of the following four: myoclonus, visual impairment or cerebellar signs, extrapyramidal or pyramidal signs, and akinetic mutism (42). If none of the test results is positive for sJCD, then the diagnosis *possible sJCD* is considered.

1.3.1 Magnetic resonance imaging (MRI) criteria

MRI illustrates a central point of clinical investigation of JCD with diffusion-weighted images (DWI) playing a significant role. The current imaging criteria for sJCD comprises hyperintense signal abnormalities in both caudate and putamen or at least two cortical lobes (temporal, parietal, occipital) either on DWI or FLAIR (49). Evidence shows DWI to be even superior to fluid-attenuated inversion recovery sequences (FLAIR) in detecting cerebral abnormalities with a sensitivity and specificity of 92–96% and 88–94% shown in several studies (2,44,45,50–54). However, A. Bizzi et al. have published a new paper in 2020 where

neuroradiologists obtained a lower sensitivity (69–82%) using the current criteria, independently of one radiologist's experience (55). Bizzi et al. simultaneously proposed new imaging criteria for the diagnosis of sJCD, showing a significantly higher sensitivity (84-98%) with unchanged specificity. These new criteria consist of at least one high signal region in the cortex (this time, the frontal lobe also included), caudate, putamen, and thalamus but excluding limbic structures and cerebellum (55:p.4).

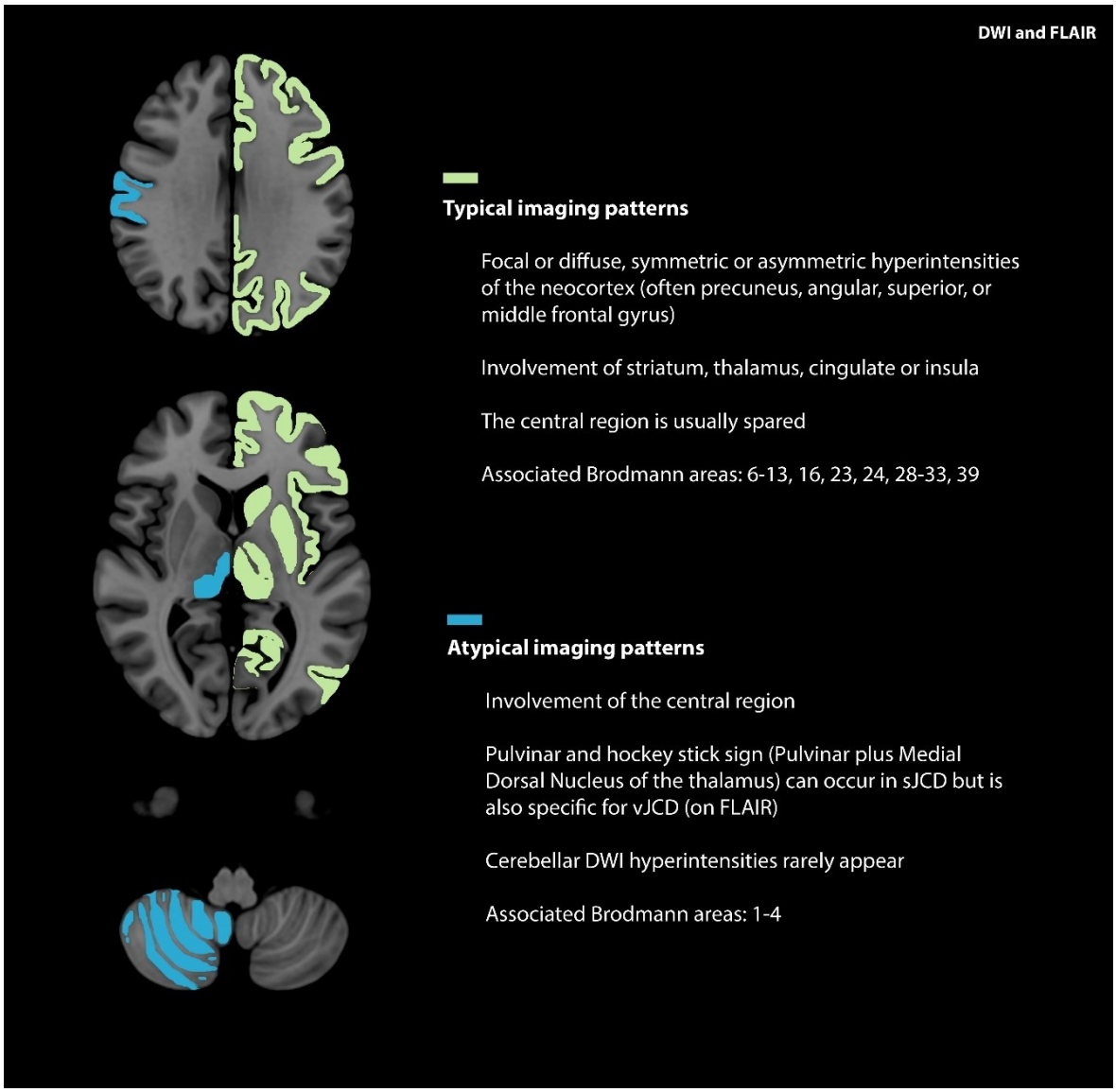

Figure 2. (2:p.7,46) Imaging patterns in sJCD. Typical (right side) and atypical (left side) patterns are seen in patients with sJCD on MRI. DWI images are more sensitive than FLAIR sequences.

DWI can be used to recognise the disease even in early stages, as it might reflect the spongiform changes in the cerebral cortex (56). Typical radiologic patterns in JCD have been allocated to structures in the brain seen on MRI in several studies (2,43,49).

Most commonly, abnormalities are interspersed diffusely throughout the cortex or basal ganglia, which can be seen best on diffusion-weighted images on MRI. There are typical and atypical lesion patterns seen on radiologic imaging associated with the disease. Usually, the neocortex is focally or diffusely involved with symmetric or asymmetric hyperintensities, consistently including the striatum. Furthermore, diffusion restrictions may also be encountered in the thalamus, the insula, or the limbic lobe (predominantly cingulate) (2,57) and always together with DWI or FLAIR abnormalities involving the neocortex. Otherwise, a different diagnosis than JCD should be considered (53). In general, the main differential diagnoses to sJCD should always be considered since JCD represents an infaust prognosis without exception. These are pathological entities that may also occur with rapidly progressive dementia and can mimic the imaging patterns of sJCD. The main differentials are Hypoxic-ischemic encephalopathy, metabolic and endocrine disorders (Hypoglycemia, Hyperammonemia, Extrapontine osmotic demyelination, Wilson disease, Wernicke disease, Manganese deposition), encephalitides or cerebellitis of infectious and autoimmune-mediated aetiology, mitochondrial disease or the more rare diseases Spectacular shrinking deficit, Hyperglycemia-Hemichorea-Hemiballism syndrome and Gerstmann-Sträussler-Scheinker disease (2). One major difference between them and sJCD would be the irreversibility of JCD in comparison to a more acute and reversible appearance of the other entities. The cortical areas around the central sulcus, associated with the Brodmann areas 1 to 4, is mostly spared but was found nonetheless to occur in atypical presentations of sJCD (2). Affections of the pulvinar, *pulvinar sign*, plus the medial dorsal thalamic nucleus, *hockey stick sign*, are seen in atypical sJCD as well but are also specific hallmarks seen in vJCD (58). In rare cases, diffusion restrictions on DWI are found in the cerebellum of patients (2).

The other variants of JCD appear similarly, thus, in order to diagnose them, a source of

prion transmission (vJCD, iJCD) or genetic mutations (gJCD) must be detected (4–6). Origins for iatrogenic JCD may still are contaminated biological samples from human cadavers transferred through neurosurgical procedures, mainly dura mater graft-associated JCD (dJCD) or human growth hormone-associated JCD (hGH JCD) (6). Nevertheless, the categorisation of these variants is blurred in terms of their clinical features. The plaque-type form of dJCD, which has plaque-type depositions of PrP^{TSE}, shows radiologic features of vJCD, and the non-plaque type those of the MM/MV1 sJCD subtype (6). For gJCD, a plethora of mutations in PRNP has been identified as being responsible for the disease.

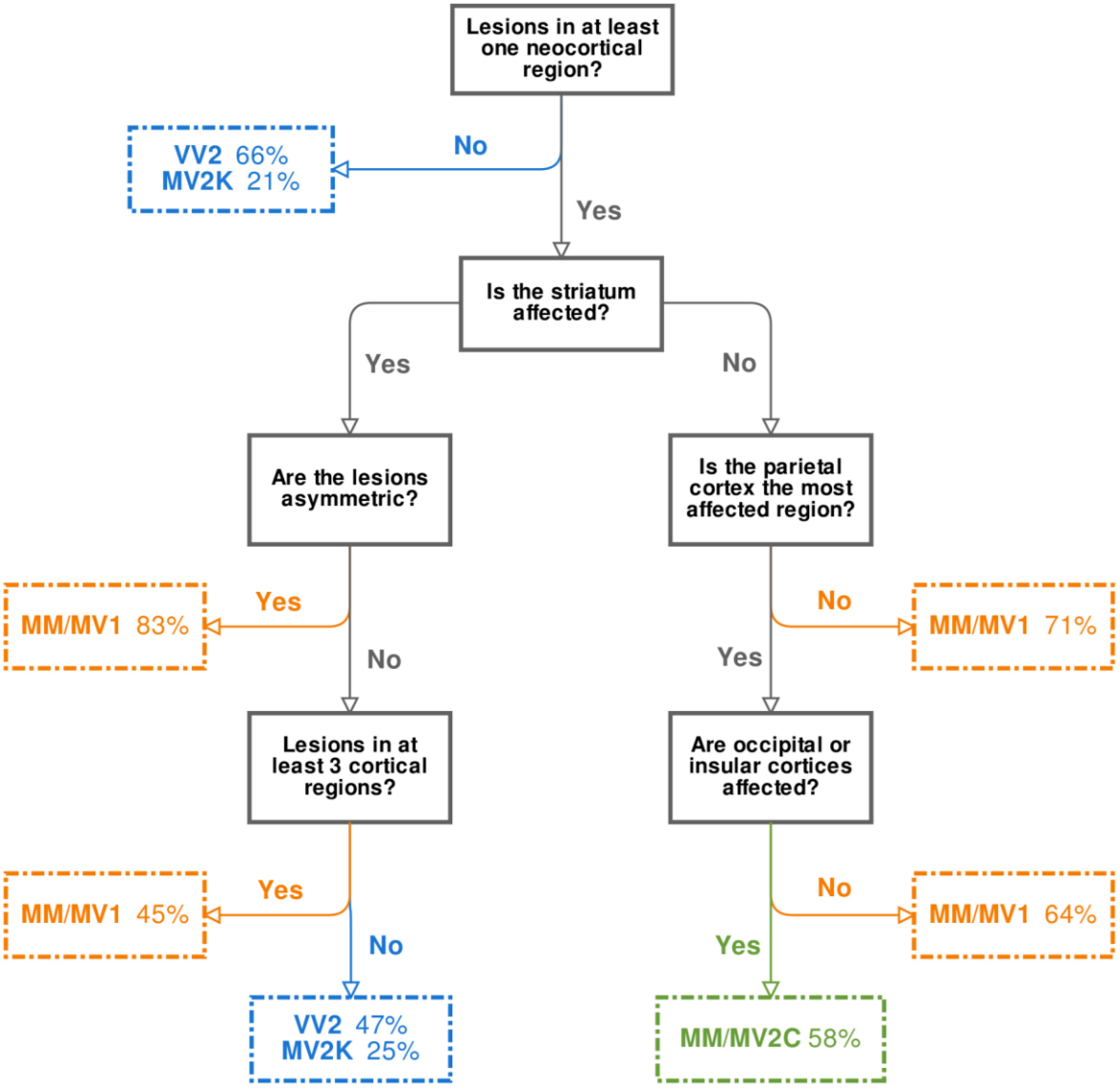

Figure 3. (59) Prion Subtype Classification Algorithm with MRI (PRISCA). This algorithm was presented by A. Bizzi, MD, at the RSNA 2018. The white boxes contain MRI questions for DWI sequences and leading to the most likely subtype.

Notwithstanding, the imaging patterns of gJCD are similar to those of sJCD, but an accurate differentiation is easily made via gene testing or anamnestic via positive family history (4).

In 2018, A. Bizzi presented a diagnostic algorithm at the 104th meeting of the Radiological Society of North America (RSNA) (59) to estimate the sJCD subtype with an accuracy of 85% only based on diffusion-weighted images. The algorithm basically uses distribution patterns of several abnormal brain lesions on DWI, which are matched with histologically approved sJCD subtypes (see Figure 3). Meissner et al. (46) published these lesion patterns for all six genotypes. Early clinical diagnosis of the subtype has the advantage of estimating the average duration of disease and survival as they differ from one another (3), and also supports epidemiologic surveillance.

1.3.2 Electroencephalogram (EEG) in JCD

The EEG is a non-invasive method in the routine diagnostics of neurology. In sJCD, it may show characteristic changes, so-called periodic bi- and triphasic sharp-wave complexes (PSWCs). Usually, PSWCs occur 2-3 months after the disease's onset, supporting the diagnosis during clinical progression (3). Although the changes might are characteristic for sJCD, this investigation's sensitivity and specificity lie at only 67% and 86% respectively (60). Another drawback is the vast list of differential diagnoses associated with PSWCs making the EEG the least significant among the diagnostic investigations currently available (60–63).

1.3.3 Cerebrospinal fluid (CSF) analysis in JCD

Analysis of a patient's CSF is of utmost importance in the clinical diagnosis of JCD. Detecting high levels of the surrogate markers 14-3-3 protein and tau protein are diagnostically conclusive in the proper clinical context (64,65). 14-3-3 is a ubiquitous protein in the central nervous system. If neuronal damage happens, these proteins reach into the liquor and can, therefore, be detected in CSF analysis. Consequently, high levels of 14-3-3 not only occur in JCD but also with all other causes for neuronal cell damage like viral infections, neurodegenerative diseases, stroke, trauma, or inflammation (3). The diagnostic sensitivity of the 14-3-3 assay is denoted with 85-95%. However, this method is only 75-96%

sensitive for sJCD (65–67,67). Furthermore, the test result's reliability appears to be dependent on the genetic subtype associated with PrP^{TSE} type 2 and longer disease duration (65).

Tau protein is another surrogate marker for sJCD, showing similar reliability as 14-3-3. This protein binds microtubules, stabilises them, and regulates the polymerisation of filaments. So-called *histologically detectable neurofilaments* are predominantly formed in Alzheimer's disease or other tauopathies. Increased levels of tau in CSF are described in sJCD as well. Furthermore, the ratio between phosphorylated tau protein and total tau protein (p-tau/t-tau) helps differentiate between JCD and Alzheimer's disease or dementia.

Other neuronal proteins have been discussed in recent publications, including amyloid b (65,68), neuron-specific enolase (69,70), S100B (69), and alpha-synuclein (71,72) but found no entry into the standard JCD protocol.

In 2011, Atarashi et al. (73) developed a new technology, denoted *real-time quaking-induced conversion* (RT-QuIC), to amplify and subsequently detect tiny amounts of PrP^{TSE} in vitro. The concept is based on the capabilities of abnormal prions aggregating and converting other PrP to PrP^{TSE}. In RT-QuIC, "soluble recombinant PrP […] expressed in E. coli is used as a substrate to amplify the minute amounts of [PrP^{TSE}]." (72:p.2) This method can be used to identify tiny amounts of PrP^{TSE} in CSF or other tissue samples of patients. In the first generation, the sensitivity and specificity of QuIC assays were declared 79–86% and 99–100% respectively (65,74,75). An improved second generation of RT-QuIC, called IQ-QuIC, rose the test's sensitivity to even 96% with shorter times of testing (76,77), giving it a substantial diagnostic and analytical potential. Therefore, this method was allocated to the CDC's (Centers for disease control and prevention) diagnostic criteria of JCD in 2017 (49).

1.4 Fundamentals of MRI

The fundamentals of magnetic resonance imaging (MRI) are among the latest technological milestones in the historical course of radiologic imaging. Until this day, eight Nobel Prizes have been awarded for research contributing to the MRI technology (Otto

Stern, Isidor I. Rabi, Felix Bloch, Edward M. Purcell, Nicolaas Bloembergen, Richard Ernst, Paul C. Lauterbur, and Sir Peter Mansfield). However, one of the main contributors of today's MRI scanners might be Raymond V. Damadian who, albeit having patented the first whole-body scanner using magnetic resonance technology and suggesting MR relaxation times could be used to distinguish between healthy tissue and cancer (78), has not received the 2003 Nobel Prize for Medicine (which causes a lot of arousal until this day in the scientific community (79)). Figure 4 depicts some of these historical discoveries.

The fundaments of MRI date back to 1922, when Stern and Gerlach experimented with atomic beams revealing ground state properties of quantum systems, known as the *Stern-Gerlach-Experiment* (80). One of these fundamental properties is called the *spin* of protons providing evidence for atoms' magnetic momentum. One and a half decades later, in 1938, Rabi also experimented with molecules sent through a magnetic field and demonstrated that these molecules could emit radio waves at distinctive frequencies and that it was possible to separate them individually (81). Bloch and Purcell augmented these discoveries to condensed matter (water and paraffin) with Purcell measuring energy absorption in his experiment (82), and Bloch recording a current induced in a nearby coil in his experiment (82), and Bloch recording a current induced in an adjacent coil from the rotation of a magnetisation vector (83). One of the other great inventions leading to what MRI is today did not come from the field of medicine but physics when Nicolaas Bloembergen published new methods to analyse molecules with laser spectroscopy (84). It was not until 1973 that Lauterbur demonstrated in examples that images could be made with nuclear magnetic resonance, calling it *zeugmatography* (85).

The first image of a human body part, a human finger, was created by Sir Peter Mansfield in 1977 (86), which took nearly five hours to generate. Together with his contributions to localise a nuclear magnetic resonance signal slice-by-slice, he was awarded the Nobel Prize jointly with Lauterbur in 2003 (87). The eighth Nobel Prize, this time in the field of chemistry, was awarded to Richard Ernst for "his contributions to the development of the methodology of high resolution nuclear magnetic resonance (NMR) spectroscopy" (88).

In these days, radiologists rely every day on MRI in their clinical practice. Without all the research and milestones being achieved leading to one of the most complex machines ever built until this day, many medical branches, not just in radiology, could not be this advanced

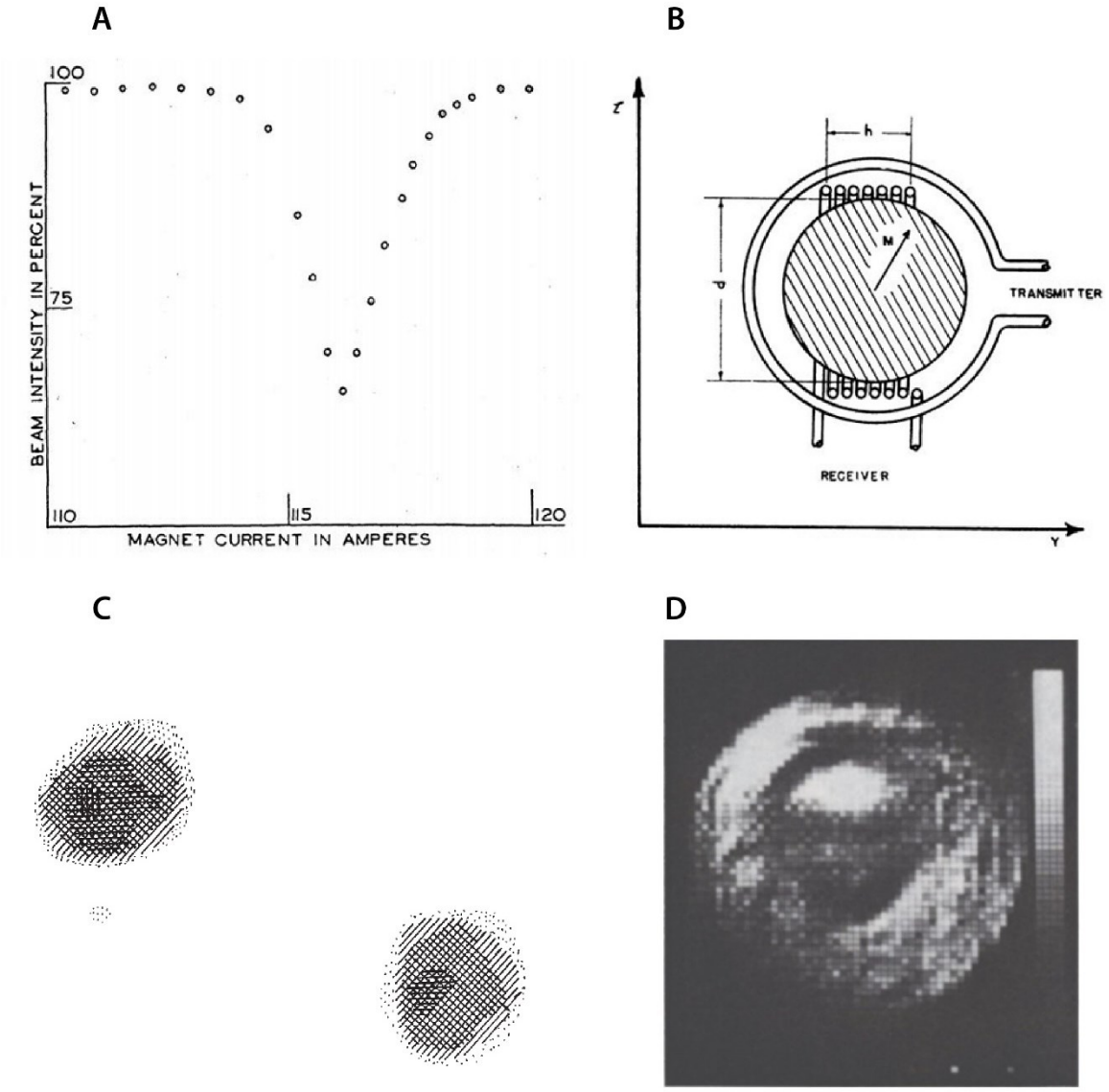

Figure 4. (81:p.1,83:p.2,85:p.1,86:p.4) Historical MRI discoveries. **A** shows Rabi's records of resonance in a magnetic apparatus of a lithium chloride beam through a vacuum chamber. **B** illustrates Bloch's apparatus: a water sample surrounded by a transmitter and receiver loops in a magnetic field. **C** Lauterbur's first MR image of two H_2O columns in 1973. **D** The first MR image of a human body part – although difficult one can identify anatomical structures like tendons, muscles or bone.

or even have ever existed in the first place. From Lauterbur's first image of a finger in coarse resolution to whole-body MRI scans, real-time MRI imaging of the heart or the development

of 7-Tesla scanners for clinical use, it took only five decades. We will probably see further innovations in the near future, augmenting physicians' competencies, and improving patients' health care.

1.4.1 Physics of MRI

Although there is a plethora of academic literature explaining the fundamental physics behind MRI, I shall summarise the basic principles before I explain the MRI sequences used for JCD, particularly for none radiologists.

Fundamentally, a clinical MR device is a massive plastic shell containing clusters of coils and a strong magnet. This magnet creates a magnetic field with a strength ranging between 0,1 to 3 Tesla (new 7-Tesla MR devices get implemented successively into routine clinical work). To understand how MR signals are produced, we have to follow some basics of quantum mechanics. Hydrogen is the most abundant element in our universe and made out of one positively charged proton, and one negatively charged electron orbiting its proton. Another property of protons is the so-called spin. When dealing with a single proton, the spin cannot be seen as an angular motion of a proton's mass (as in the physics of classical mechanics) but as a quantum-mechanical characteristic. It gives protons a magnetic momentum that enables them to align in a parallel or an antiparallel orientation in the presence of an external magnetic field. In MR imaging, one is dealing with multiple protons. Realigned spins sum up to a net magnetisation vector orientated parallelly to the magnetic field (the parallel orientation outweighs the antiparallel state due to a small energetic difference favouring the parallel state). This magnetic vector allows one understanding the physics behind MRI in a classical mechanical way with imagining protons as spinning tops for simplification purposes.

In a spinning top, gravity continually tries to change its rotational axis laterally. As with spinning tops, proton spins make this evasive movement in a magnetic field, called *precessional motion.* One cannot observe this motion, but it is possible to measure the position of the vector of net magnetisation. This movement happens in a specific so-called

Larmor frequency, which is precisely proportional to the magnetic field strength B_0. The following formula determines it:

$$\omega_{Larmor} = \gamma \cdot B_0$$

ω_{Lamor}: Larmor frequency in Megahertz (MHz) | **γ**: Gyromagnetic ratio in Megahertz per Tesla (MHz/T) (this is a constant describing the ratio of a magnetic impulse to an angular impulse of a system or particle – in our case a proton) | **B_0**: Magnetic field strength in Tesla (T)

In MRI, the Larmor frequency is essential since a high-frequency transmitter sends electromagnetic waves in exactly this frequency to excite the spins of hydrogen protons. If a radiologist wants to generate an MR image, first, the proton spins have to be aligned in the MR's magnetic field to build up a longitudinal magnetisation of their spins, which happens at the moment a patient is positioned in the MR tube. This longitudinal magnetisation is the sum of magnetic moments of all free protons in a patient. With the abovementioned high-frequency transmitter, the vector of longitudinal magnetisation is flipped from a longitudinal into a transversal layer. After the transmitter is turned off, this vector moves back into alignment of the magnetic field. Since protons are charged particles, their movement induces a voltage in a receiver coil, which is the actual MR signal.

The MR signal passes through a post-processing phase consisting mainly of a mathematical method called *Fourier transformation* to generate an image eventually. However, an image's contrast is dependent on three parameters:

- the ***T1-time*** (or *longitudinal relaxation*) which is the time that the spins need to realign in the magnetic field after they got excited
- the ***T2-time*** (or *transversal relaxation*) representing the time the spins need to lose their phase synchronisation. When the vector of net magnetisation is flipped into a transversal layer, they continue spinning synchronically. Since the spins themselves interact with each other, they exchange energy leading to tiny magnetic inhomogeneities which lets the spins gradually precess with different frequencies. These inhomogeneities successively reduce their magnetic vector, decreasing the MR signal and can, therefore, be measured.

- The ***proton density*** of the examined tissue

Consequently, different tissues have very different values of these three properties leading to different MR signals. Ergo, soft tissues like brain tissue and connective tissue are better distinguishable from each other by MRI than by computer tomography (CT) since their densities are almost the same but not their composition. By weighting T1, T2 or proton density differently, a radiologist can use several MR sequences with different diagnostic value.

1.4.2 Sequences in JCD

The primary sequences to diagnose and evaluate JCD are DWI, Apparent diffusion coefficient maps (ADC), FLAIR and T2. It was not until 1988 that MRI was considered a diagnostic marker of early JCD (89). In this study, T2 was the first sequence recognising high-signal intensities in basal ganglia of patients suffering from JCD. Along with it, FLAIR sequences were also used but with low sensitivity (50). Shiga et al. (50) were the first to evaluate DWI sequences to be diagnostically more conclusive than T2 or FLAIR, particularly in earlier disease stages.

DWI is utterly different from T2 or FLAIR sequences since it measures water molecules' movement in tissue voxels. Two features can cause a high signal in DWI on brain images compared to normal brain matter: the first illustrates a lower diffusion coefficient and therefore reduced integrity of this particular region. Secondly, T2-prolongation may also alter DWI signals which would also show up in the FLAIR or T2 images, but it was shown that high-signal abnormalities occur more often in DWI sequences than in T2 or FLAIR images in patients with JCD. This observation was attributed to vacuolation and reactive astrocytic gliosis leading to diffusion restrictions (90), which could explain the dominant role of DWI sequences.

The following formula determines the DWI signal:

$$S_{DWI} = S_{T2^*} \cdot e^{-b \cdot ADC}$$

S_{DWI}: the signal intensity on the greyscale DWI | **S_{T2*}**: the baseline signal | **-b**: a factor representing the timing of gradients during the DWI sequence | **ADC**: the diffusion coefficient

By reading this formula, one notices that DWIs are basically T2-weighted images with a diffusion component. Consequently, that explains why T2-relaxation time and diffusion are the two features generating the DWI signal. T2* (spoken as "T2-star") reflects that the scanner does not perfectly refocus during the DWI scan making the signal more susceptible to magnetic field inhomogeneities causing signal loss eventually. This is particularly the case in *gradient-echo* sequences. However, another standard pulse method called *spin-echo* reverses this effect. In spin-echo sequences, after an initial 90° pulse is applied that turns the vector of net magnetisation into a transversal plane, a 180° pulse follows after half of the echo time (TE) so that "faster" precessing spins are put behind "slower" spins which gradually turns them back into phase. DWI images can be generated with both sequences respectively or in combination with each other (as it was done in this thesis). The b-value is the factor that the radiologist controls. A higher b-value causes a more substantial diffusion weighting leading to less base signal. Restricted diffusion represented by ADC does just the opposite: As it is a negative exponent in the above-shown equation, the DWI gets brighter with lower diffusion of free water.

Subsequently, one major problem with DWI is that high-signal abnormalities are not only caused by diffusion restriction, which is the component that one wants to find out in DWI, but can also occur when the T2*-image (or T2-image when using spin-echo sequences) itself is bright (called *T2-shine through*). To solve this problem, the same scan is repeated another time but with a b-value of 0. This creates a pure T2*-image because, with a b-value of 0, there is no diffusion-weighted component. Subsequently, by removing the T2-signal from our merged scans a so-called *Exponential diffusion coefficient map* (EDC) is produced. In order to get an ADC map, one has to solve the following formula for *ADC*:

$$EDC = e^{-b \cdot ADC}$$

The result is an inverted image to the DWI scan, showing lower signal in areas with restricted diffusion while these areas appear bright on DWI without any T2-shine through effects.

1.5 Brodmann areas

The German neuroanatomist Korbinian Brodmann published his book "Vergleichende Lokalisationslehre der Grosshirnrinde in ihren Prinzipien dargestellt auf Grund des Zellenbaues" in 1909, revealing his studies on the cytoarchitectural division of cortical areas (91).

At the beginning of the 20th century, neuroanatomists and pathologists required a standardised histological nomenclature of the brain's surface. K. Brodmann solved this task by defining forty-seven distinct cortical areas, called *Brodmann areas*, based on six cellular layers differing in density and architecture in every region (91), shown in figure 5. His classification did not only ground on pathological observations but rather ontogenetic considerations. As Brodmann stated in his preamble (91):

> *"I was therefore forced to put aside the overly complicated and confusing human brain for the time being and try to gain an insight into the blueprint of the cortex cerebri from ontogenetic conditions and simple forms."* (translated quotation, p. III)

Hence, a plethora of different mammal brains were analysed to compare their cellular architecture with that of human brains (91). This makes it possible to describe JCD on an ontogenetic and phylogenetic level with radiologic imaging.

With his work, Brodmann laid the basis for stereotactic atlases being indispensable for neurosurgical interventions and research nowadays. In 1988, J. Talairach et al. (92) assigned the Brodmann areas to neuroanatomical regions on a standardised brain template, creating the first stereotactic atlas for surgical use. However, the Talairach Atlas brain is mostly replaced by the *Montreal Neurological Institute* coordinates (MNI) in everyday practise (93). There are several reasons for this: the MNI space illustrates an average 3-D brain image

template, while for the Talairach brain photographs of brain specimens were used to label neuroanatomical landmarks on them, rather approximately, by using Brodmann's drawings (93). In the current MNI standard (ICBM-152) brain volumes of 152 patients were averaged after registering them to the initial MNI-305 template, which itself is an average brain template of 305 brain volumes (93). Lancaster et al. (93) have shown that brain volumes registered to MNI space and Talairach space are significantly different. Both templates can be used for spatial normalisation of human brain volumes in order to prevent anatomical variability, like in this thesis. However, the methods differ: in MNI space, the volumes are automatically fitted to the 3-D brain templated, but in Talairach space, a landmark-based

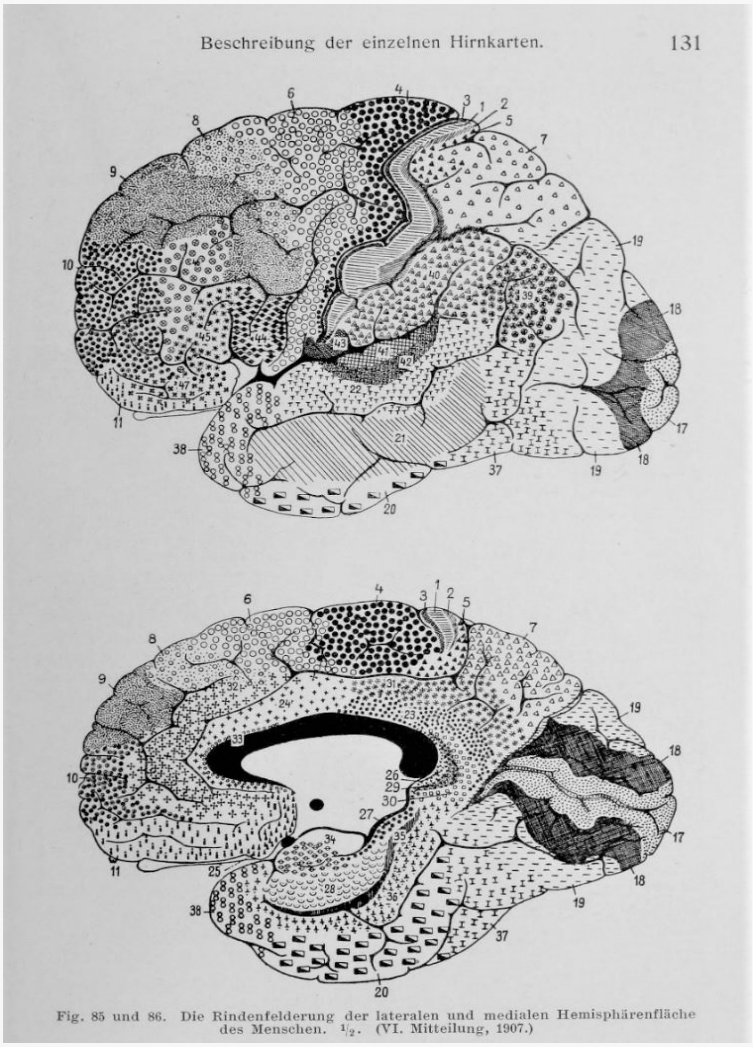

Figure 5. (91:p.131) Brodmann areas. Brodmann's original drawings of his areas and brain maps (ger. "Hirnkarten")

approach is used (93). Also, the coordinates of reference between both templates differ slightly, making it difficult to compare studies (93). Although there are different approaches available to transform MNI into Talairach space and vice versa, these methods are just approximations since there is no MRI scan of a Talairach brain existing (93,94).

1.6 Evolution of the human cortex

As the human brain evolved, it changed dramatically regarding its cytoarchitectural setup from three to six distinct neuronal cortical layers. Therefore, the human cortex can be categorised into *neocortex* (six layers), *allocortex* (three layers) and *mesocortex* (transitional zone four to six cellular layers) (see neuroanatomical textbooks). In human, the cerebral cortex consists of 85% of neocortex, 5% of mesocortex and 10% of allocortex (95,96). The allocortex can be subdivided into *archicortex* and *paleocortex*, representing the evolutionary oldest cortical regions. As the name implies, the neocortex (also called *isocortex*) embodies the newest development of cortical evolution in humans. Since Brodmann's classifications were based on a six cellular structure, his areas, strictly speaking, only reflect the neocortex (91). However, because some cortical territories were arbitrarily assumed, certain Brodmann areas are located in the mesocortex or allocortex, although a three cellular setup defines the latter. For instance, some parts of the parahippocampal cortex are assigned to Brodmann area 36; the cingulate gyrus can be found in area 23 – 25, 30 -32, both portraying the mesocortex. In the allocortex, for instance, the entorhinal region can be considered as area 34.

Consequently, in order to examine the human cortex in matters of phylogenetics, one may not use Brodmann areas, respectively, the Talairach atlas. A better method would be an anatomical approach, particularly for radiological imaging, in form of an anatomically labelled template based on MNI space brains. The *Automated Anatomical Labelling* atlas (AAL) illustrates one of these templates used in this thesis (97). With this anatomical atlas, it is possible to assign JCD lesions on DWI scans to distinct anatomical regions and, therefore, enables a phylogenetic classification of these lesions.

1.7 Connection concepts and Brodmann

Brodmann areas reflect cortical regions with distinct functionalities. These functionalities occur due to various white matter pathways being merged into fibre tracts that can be allocated to Brodmann areas (98). In 1970, Jones and Powell (99) were one of the first to systematically investigate potential association cortices and their underlying white matter connections by causing small damage to the brains of rhesus monkeys and then examining these brains for atrophies of cortical areas apart from the region of damage (99). Jones et al. stated that sensory pathways could be converged into three sensory systems: somatic, visual, and auditory (99).

Nowadays, research has shown that the human brain system pathways are far more complex. The *Human Connectome Project* (HCP), initiated in 2010, was a five-year project to explore the fibre connections not only of healthy human brains but also of brains with disorders (100). It has shifted to a new project, called the *Connectome Coordination Facility* (CCF), aiming to support further research projects in this field (100). In a publication of Swanson et al. (101), the complexity of the cortical connections is illustrated, showing the network of commissural and association connections in the brains of rats. These connections arise from fibres connecting the brain's neurons, which reflect different cerebral regions' communication with one another (101). These fibres follow certain architectural and connection concepts, which were thoroughly brought together by D. Pandya et al. (102). The vast amount of neuroanatomical and histological research on macaque monkeys' brains forms the foundation for these concepts. It led to the subdivision of the cerebral cortex into an auditory, motor, somatosensory and visual system having reciprocal connections with the paralimbic cortex (PL), the prefrontal cortex (PF) and the so-called *multimodal cortex* (MM) (102), processing different sensory inputs. These four systems are interconnected with the PL, PF and MM in a specific way, described as the concept of *core-root-belt* lines grounded on the idea of the dual origin concept (102). It has to be mentioned that the gustatory, olfactory, vestibular system and amygdala also appear to follow the abovementioned

Table 3	Assignment of fibre tracts to Talairach atlas	
Fibre tract	**Connected areas**	**Assigned Brodmann areas (Talairach)**
Superior longitudinal fasciculus (SFL)/Fronto-occipital fasciculus (FOF)	SMA, Premotor cortex, Prefrontal cortex ◄► Parietal areas (PEc, PGm, PG, 31, PE, POa, Opt, PF, PFG, Pfop)	5-9, 31, 39, 40, 44, 46
Inferior fronto-occipital fasciculus (IFO)	Primary visual cortex, Visual association cortex, V3 ◄► Prefrontal cortex, Frontopolar area, Broca`s area	10, 17-19, 45, 46
Uncinate fasciculus (UF)	Superiorostral temporal cortex, Broca`s area ◄► Ventrolateral prefrontal cortex, Cingulate cortex	10, 13, 24, 25, 32, 36, 38, 45-47
Arcuate fasciculus (AF)/Extreme capsule (EmC)	Superior temporal cortex, Insular cortex, Primary auditorial cortex Parahippocampal cortex, Wernicke's area, Broca's area ◄► SMA, Premotor cortex, Prefrontal	8, 9, 13, 22, 36, 41, 45, 47
Middle longitudinal fasciculus (MdLF)	Temporal polar area ◄► Precuneus, Cuneus, Area around the parieto-occipital sulcus	7, 17, 18, 19, 38
Cingulate bundle (CB)	Prefrontal cortex, Orbitofrontal area, Insular cortex ◄► Parahippocampal cortex, Parietal areas (PG, Opt), Cingulate cortex	8, 9, 11, 13, 25, 30-34, 36, 39, 46
Inferior longitudinal fasciculus (ILF)	Parietal areas (POa, Opt), Occipital lobe, Superior temporal cortex ◄► Inferior temporal cortex, Parahippocampal cortex	7, 17-19, 36

The ◄► symbol indicates a connection between the named areas in both ways via their dedicated fibre tracts

concepts but embody an evolutionary much older area of the human brain (as they belong to allocortical or periallocortical regions) and therefore were not considered in the following analyses as there is no plain core-root-belt concept apprehensible for these systems (102). A system's *core* illustrates its primary sensory cortex, the *root* all secondary receptive areas and the *belt* lines incorporate a system's association pathways towards other cortical regions (PL, PF, MM) (102). It has to be mentioned that these three fundamental fields have interconnections (core-core connections, root-root connections, root-belt connections). All these pathways represent a functional blueprint of short-range (U-) and long-range fibres, which belong to association fibres (cortex-cortex connections) (103). In this thesis, additionally, the involvement of long-association pathways in sJCD patients was inspected separately. These were likewise divided into different bundles and allocated to the brain regions they connect, in former studies (104,105).

In terms of JCD, association fibres might have a significant role in the distribution of lesions over the cortex as animal models suggest an axonal transport of PrP^{TSE} between brain

regions (106). In recent studies, white matter involvement in JCD was observed, supporting the theory of a primary or secondary effect on axonal pathways by PrP^{TSE} (107,108). At the time of writing this thesis, no known publications that examine a potential pattern between MRI lesions of the cortex and those fibre bundles in JCD patients exist.

For this purpose, the following cortical pathways/association fibres with regard to their origins were taken into account:

Long-range fibres:

- *Superior longitudinal fasciculus* (SLF) (all three subcomponents) and *fronto-occipital fasciculus* (FOF) for the parietal lobe
- *Inferior fronto-occipital fasciculus* (IFO) for the occipital lobe
- *Inferior longitudinal fasciculus* (ILF) for the occipitotemporal region
- The *uncinate fasciculus* (UF) and the *arcuate fasciculus* (AF) plus *extreme capsule* combined for the temporal lobe
- *Middle longitudinal fasciculus* (MdLF) connecting the temporal pole with the parieto-occipital region through the angular gyrus
- *Cingulate bundle* (CB) for the parahippocampal region

Cortices (Dual Origin Concept):

- Auditory System
- Motor System
- Somatosensory System
- Visual System

The affinity of these bundles to their cortical areas of origin or termination and the allocation to Brodmann areas shown in Table 3 and 4 were determined by reference to several neuroanatomical publications on this topic (98,102–105,109–114).

Table 4	Assignment of cortical systems to Talairach atlas	
Cortical system	**Areas**	**Assigned Brodmann areas (Talairach)**
Auditory system	**Core**: A1-KA	41
	Root: Pro, PaI, ProK, reIt	22, 38
	Belt: TS1, TS2, TS3, PaAlt, Tpt	10, 22
	MM: TPO, Insula, Cingulate, Parahippocampal gyrus	13, 23, 30, 36, 41
	PL: Cingulate, Parahippocampal gyrus, Retrosplenial cortex, Insula	13, 23, 30, 36
	PF: 13, 11, 10, 25, 14, 47/12, 8Ad, 9/46, 45	8, 9, 10, 11, 13, 25, 45, 46
Motor system	**Core**: MI	4
	Root: MII, CMA, ProM	4, 6
	Belt: Premotor (6V, 6D), Rostral Parietal	5, 6, 7, 39, 40
	MM: Insula, TPO, PGm, PG, Poa, 13	13, 31, 39, 40, 41
	PL: Insula, Cingulate, 31, 13	13, 23, 30, 31
	PF: 46, 9/46v, 8, 9, 45, 47/12, 13, 11	8, 9, 11, 45, 46, 47
Somatosensory system	**Core**: SI	1
	Root: SII, PV, SSA	5
	Belt: 1, 2, 5, PF	1, 5, 40
	MM: PG, TPO, Insula, Cingulate gyrus, Parahippocampal gyrus	13, 23, 30, 36, 39, 41
	PL: Cingulate, Parahippocampal gyrus, Caudal orbital cortex, Retrosplenial cortex, Insula	11, 13, 23, 30, 36
	PF: 47/12, 9/46v	9, 46, 47
Visual system	**Core**: V1-V2	17, 18, 19
	Root: Tea, FST, MT, V4t, MST	18, 19
	Belt: TE1, TE2, TE3, TEo, V4, V3	18, 19, 21, 22, 40
	MM: PG-Opt, Insula, Cingulate, Parahippocampal gyrus, TPO	7, 13, 23, 30, 36, 41
	PL: Cingulate, Parahippocampal gyrus, Insula	13, 23, 30, 36
	PF: 8Av, 45, 47/12, 11, 8Ad, 6, 9/46d, 8B	6, 8, 9, 11, 45, 46, 47

MM - Multimodal cortex; **PL** - Paralimbic cortex; **PF** - Prefrontal cortex

Material and Methods

2.1 Patients

All patient data were collected via the hospital information system's database over a period of ten years. The search was done for all patients in whose course of the disease the suspected diagnosis Jakob-Creutzfeldt disease was established at least once. The database search revealed 15 patients, four of whom were rejected due to a lack of MRI data. Another patient was removed as the MRI scans did not comply with the JCD imaging criteria. All patients had a negative history of familial cases of JCD or exposure to known prion-contaminated neurosurgical instruments, tissue grafts, and pituitary extracted hormones.

The patients were classified according to the current diagnostic criteria (49) as clinically probable, possible or 'not' JCDs, based on the clinical information and exams by neurologists of the University Clinic of Graz. Two experienced neuroradiologists (E.H. and J.S.) interpreted MRI scans. CSF samples were determined by the Clinical Institute of Neurology, Vienna, for 14-3-3 protein; EEGs were reviewed by neurologists of our university for PSWCs. An autopsy was performed, if available, in the diagnostic centre at the Institute of Pathology (Medical University of Graz).

2.2 Image Acquisition

A total of 40 MRT scans from 10 patients were evaluated (10 T2-weighted, 10 FLAIR, 10 DWI and 10 DWI/ADC). A 1. 5 Tesla system of a Siemens Magnetom Espree was used. All scans were acquired in the anterior commissure-posterior commissure with a slice thickness of 5mm with no gap, a matrix of 192x100 pixels and a field of view of 230mm. For diffusion-weighted MRI, the diffusion gradients were successively and separately applied in three orthogonal directions for a total acquisition time of 97 seconds. Trace images were then generated, and ADC maps were calculated with a dedicated software tool (Syngo, Siemens).

Table 5 **Radiologic sequence parameters**

Sequence	Repetition time (TR)	Echo time (TE)	Inversion time	Diffusion gradient b value
Diffusion-weighted (DW) single-shot spin echoplanar sequence	5000 ms	114 ms	65 (36–83)	0 - 1000 s/mm^2
Fluid-attenuated inversion recovery (FLAIR)	9770 ms	99 ms	2200 ms	-
T2-weighted turbo spin echo sequences	4500 ms	85 ms	-	-

The respective scans were analysed by experienced neuroradiologists (E.H. and J.S.) with focus on DWI and FLAIR hyperintensities (or signal attenuation in the ADC) in caudate nucleus and putamen (Neostriatum), in cortical regions (frontal, parietal, temporal, occipital, insula, cingulate gyrus) and thalamus (all nuclei, "pulvinar" sign and "hockey stick" sign (58)) in accordance to the above mentioned diagnostic criteria (chapter 1.3.1 "Imaging patterns"). Since JCD was cautiously made a suspected diagnose in most cases, the overall goal was to determine imaging patterns typical for JCD (2). Further differential diagnoses

were considered in addition to JCD (such as stroke, hypoxia or encephalitis). In patients who were examined several times, MRI images at the time of clinical diagnosis for JCD were used.

2.3 Data Analysis

2.3.1 Image preprocessing

The acquired images underwent a specific preprocessing algorithm using the neuroimaging software SPM12 (Statistical Parametric Mapping) (115) on *MATLAB* R2020a (116). The computational procedures carried out in this software were mandatory to reduce the data variability and register all MRI sequences to the MNI space. All DICOM files were converted into NIFTI files and underwent realignment, coregistration and spatial normalisation (see Figure 6). Firstly, the DWI scans were imported into SPM12 and realigned using the default settings for estimation and reslice processes. During this realignment, an average matrix of the DWI scans was generated. Since the relaxation time (TR) of the DWIs was 5000ms, a slice-timing correction with a 79x95x79 matrix (slice order 1x79) was done. In the next step, the average matrix of the realigned DWI scans and a high-resolution anatomical T1 image of one of the subjects were coregistered. To verify the coregistration's success, certain anatomical structures (ventricles, borders of the cortex, basal ganglia, commissures) were compared between the average matrix and the coregistered T1.

A joint histogram illustrating the normalisation process's mutual information before and after the transformation was obtained, displayed in Figure 6. Thereupon, tissue probability maps of six tissues (grey matter, white matter, CSF, soft tissue, bone, other) were created out of the coregistered T1 to generate a deformation field for the final normalisation step. The settings "Save Bias Corrected" and "Deformation Field: Forward" were applied during this computation. Additionally, a new origin was set in the centre of the anterior commissure for all prior DWI scans which finalised all preparatory steps.

Finally, the slice-time corrected realigned DWI scans were normalised into standardised MNI space using SPM's default settings for estimation and reslicing again.

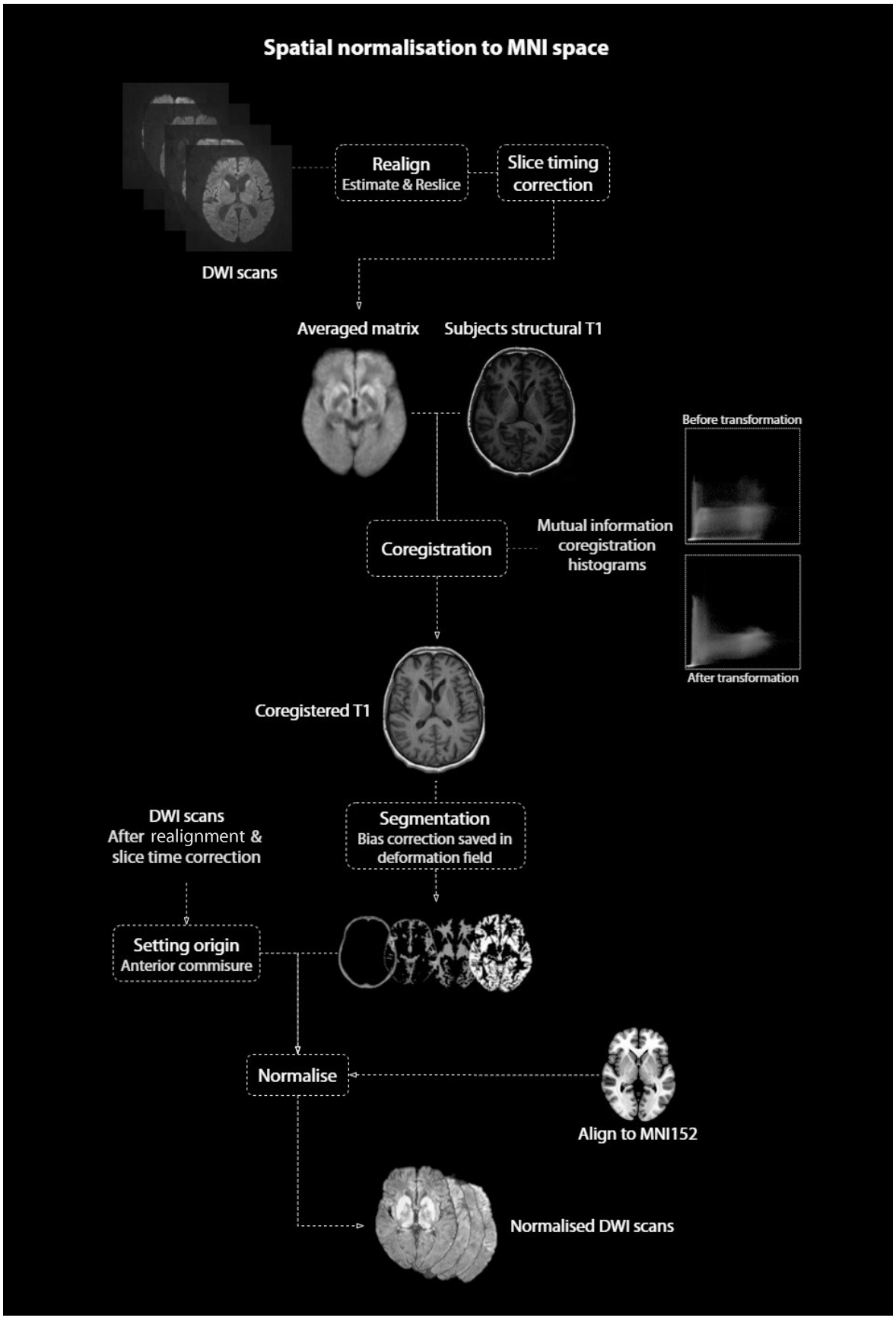

Figure 6. Spatial normalisation to MNI space. This flowchart illustrates every preprocessing step until normalisation into standardised MNI space in SPM12.

2.3.2 Segmentations

The JCD lesions displayed on the normalised DWI scans were manually segmented using the neuroimaging tool *MRIcroGL* (version: 1.2.20200331) (117). To determine DWI signal abnormalities as "real" diffusion restrictions, ADC maps were adduced for confirmation. The created volumes of interest were again converted into NIFTI files for further processing.

With a MATLAB code being written to extract the MNI space XYZ-coordinates of the segmentation masks, data tables were automatically generated filled with those coordinates in Excel (Office 365). The code can be obtained from the Appendix.

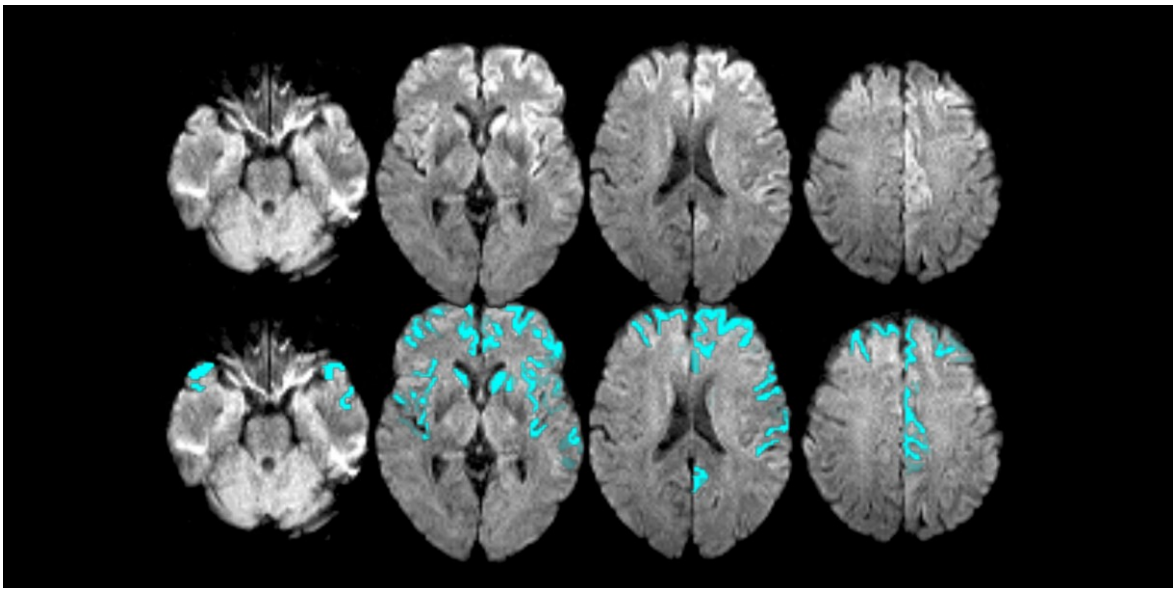

Figure 7. Example of segmentation of sJCD lesions in one subject.

2.3.3 Automatic allocation to atlas templates

In order to allocate the JCD lesions to the AAL atlas and Brodmann areas, Y. Chuang created the *label4mri* package (118), which can classify MNI coordinates to their specific regions on the AAL or Talairach atlas. In this thesis, this package was executed in the *RStudio* (R 4.0.2) environment (119). The abovementioned Excel files were loaded into a self-written R script and automatically classified via the label4mri package (see Appendix). It is essential mentioning that the label4mri package uses the AAL 2 and Talairach atlas of MRIcron (120). Especially for the Talairach atlas, which is not based on MNI coordinates (see chapter 1.5),

it was transformed into the MNI space by a usually used transformation method proposed by Lancaster et al. (93). Therefore, the MNI coordinates were allocated to the Brodmann areas using the Talairach atlas being transformed into the standardised MNI ICBM-152 space. The whole workflow of the brain area classification process is displayed in Figure 8.

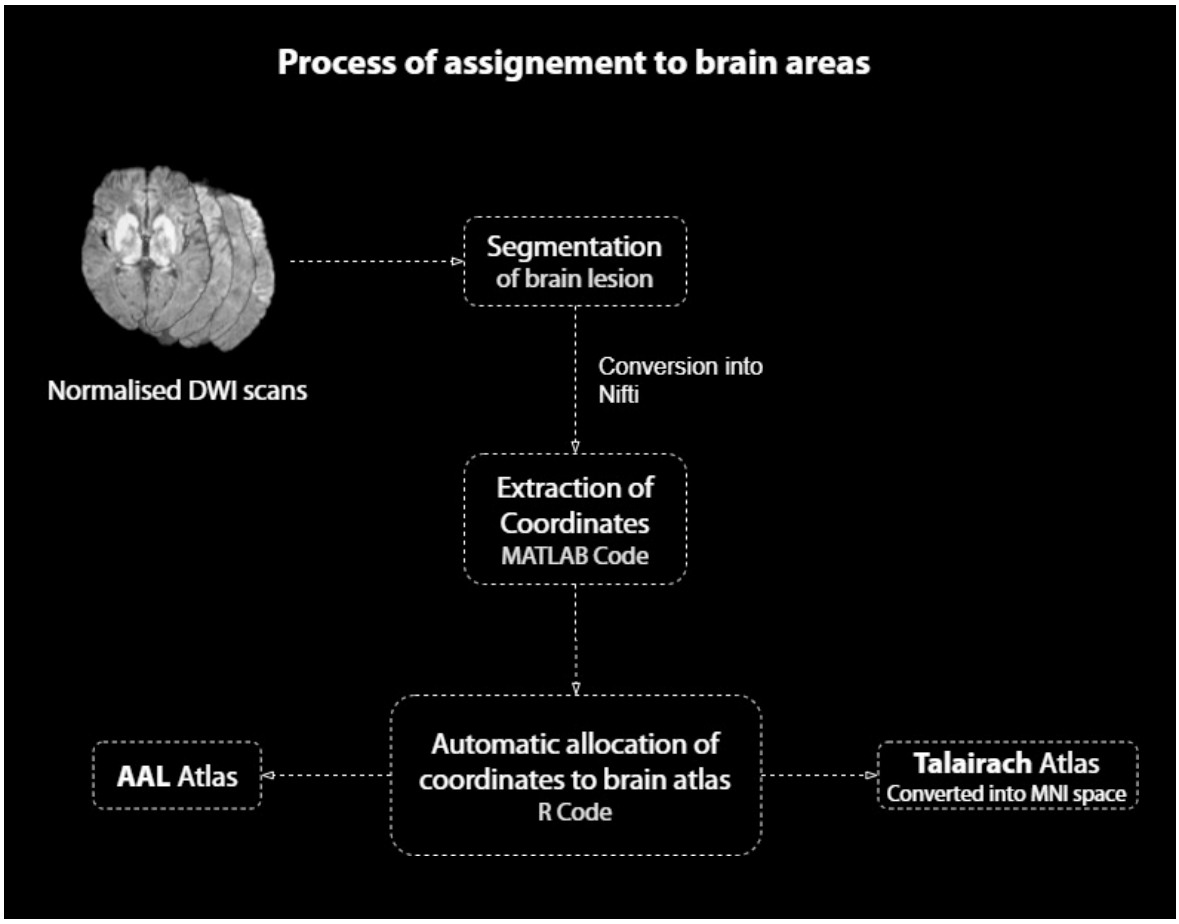

Figure 8. Process of assignment to brain areas.

2.3.4 Statistical analysis

The statistical analysis was performed on a PC running a Windows 10 platform. Two R scripts were written for the AAL and Brodmann file respectively, which can be obtained in the Appendix. A *Welch Two Sample Student's t-test* was carried out to examine a potential difference in the distribution of lesions between the left and right side of the subject's DWI scans. Volumes of lesions were calculated by taking the number of voxels multiplied with the normalised scans' voxel size (2x2x2 mm). Three-dimensional surface mesh calculations were executed using MRIcroGL. To compare the distribution of lesions between the three

phylogenetic areas, a null hypothesis was constructed: If sJCD lesions are homogeneously distributed over the human cortex, none of the three phylogenetic areas would be affected stronger or lesser. Since these three areas share a different percentage on the human cortex (95,96), their absolute volumes were relatively adjusted to the isocortex by considering the respective portion of the meso- and allocortex. By multiplying the reciprocal values of their percentages and putting them into a ratio with the isocortex, all phylogenetic cortices were volume adjusted. With these steps, the null hypothesis could be investigated. The alternative hypothesis would be that the sJCD lesions are heterogeneously distributed over the cortex with an increased incidence in one phylogenetic area compared to the others. If the ratio's value is greater or smaller one (>1, <1) in one of the cortices, the alternative hypothesis has to be considered.

Furthermore, all lesions were assigned to the auditory, motor, somatosensory and visual system via another R script (see Appendix). Subsequently, all lesions were volumetrically plotted and statistically analysed. Since the volumes were not normally distributed a *Kruskal-Wallis* test followed by a pairwise *Wilcoxon rank* test with *Bonferroni correction* was used to search for a significant difference between the four systems and their subsystem.

Results

3.1 Clinical assessment

Of the ten patients, all had DWI sequences available which, together with the clinical presentations, fulfilled the current diagnostic criteria for sJCD in every case. Six female patients and four male patients showed rapidly progressive dementia (mean [SD] age, 64.7 [13.0]). PSWCs could be displayed on EEG in three patients. High 14-3-3 protein signals were measured in six out of ten patients. Further symptomatic related to sJCD is listed in table 5. The median time from the initial diagnosis of sJCD until a patient's death was 37 days. On MRI, DWI signal hyperintensities were found predominantly in the frontal lobe and polar region, parietal lobe, temporal lobe and polar region, insular cortex, and basal ganglia. One patient's DWI scan revealed a hockey stick sign in the thalamic area; another

Table 6			Patient characteristics				
Case	Sex	Age	PSWCs (EEG)	14-3-3 protein	Rapidely progressive dementia	Other symptoms	Time of initial diagnosis to exitus (in d)
1	F	70	+	+	+	Vertigo, ataxia, cerebellar signs	37
2	M	75	+	+	+	Myclonus, hemiparesis, visual/cerebellar signs, extrapyramidal signs	57
3	F	61	-	+	+	Dystonic tremor, Parkinson syndrome, cerebellar signs, extrapyramidal signs	415
4	F	77	+	+	+	Myoclonus, hemiparesis, akinetic mutism, apraxia	33
5	M	48	-	-	+	Cerebellar signs, extrapyramidal signs	35
6	F	77	-	n.a.	+	Akinetic mutism, pyramidal signs, visual signs	n.a.
7	M	52	-	n.a.	+	Myoclonus, cerebellar signs, extrapyramidal signs	n.a.
8	F	77	n.a.	n.a.	+	Cerebellar signs, apraxia	n.a.
9	F	43	-	+	+	Myoclonus, akinetic mutism, ataxia	n.a.
10	M	67	-	+	+	Ataxia	n.a.

patient showed diffusion restriction in the right motor cortex, concordant to his hemiparesis on the left side on clinical examination. Another patient showed basal ganglia involvement only. Some examples of remarkable DWI scans are portrayed in Figure 9.

3.2 Distribution of sJCD lesions over phylogenetic cortices

The AAL labelling of the lesions revealed no significant difference in distribution between the left and right side of the brain, neither for lesions in the isocortex (t [p-value] t-test, 0.70 [0.50]), the mesocortex (t [p-value] t-test, 0.88 [0.4]), nor in the allocortex (t [p-value] t-test, -0.1 [0.92]). Most of the volumes of sJCD lesions are located in the isocortex (mean [SD] volume, 81804.8 [37669.1]), followed by the mesocortex (mean [SD] volume, 9304.8 [6072.2]), and allocortex (mean [SD] volume, 135.2 [142.3]).

The results of the phylogenetic classification are listed in table 6 and illustrated in figure 10. The volume adjusted ratios revealed the following results: The mesocortex to isocortex ratio is 1.92 (SD, 1.33), and the allocortex to isocortex ratio is 0.02 (SD, 0.03).

Consequently, this means the alternative hypothesis of a heterogeneous distribution of sJCD has to be considered, with lesions occurring almost twice as often in the mesocortex and with virtually no involvement of the allocortex (see figure 11).

Table 7	Phylogenetic volumes of lesions			
Phylogenetic cortex	Volume (SD) in mm^3	Volume left side (SD) in mm^3	Volume right side (SD) in mm^3	P value
Isocortex	81804.8 (37669.1)	44685.6 (28164.3)	37119.2 (19921.3)	0.50
Mesocortex	9304.8 (6072.2)	5412.8 (5049.9)	3892.0 (2142.0)	0.40
Allocortex	135.2 (142.3)	65.6 (74.0)	69.6 (105.0)	0.92

The P values are from the Welch Two Sample Student's t-test between the volumes of the left and right side.

3.3 Involvement of association cortices in sJCD

Most sJCD lesions are located in association cortices of the SLF (mean [SD] volume, 34.9% [14.9%]), followed by the CB (mean [SD], 31.2% [13.0%]) and UF (mean [SD] volume, 28.3%

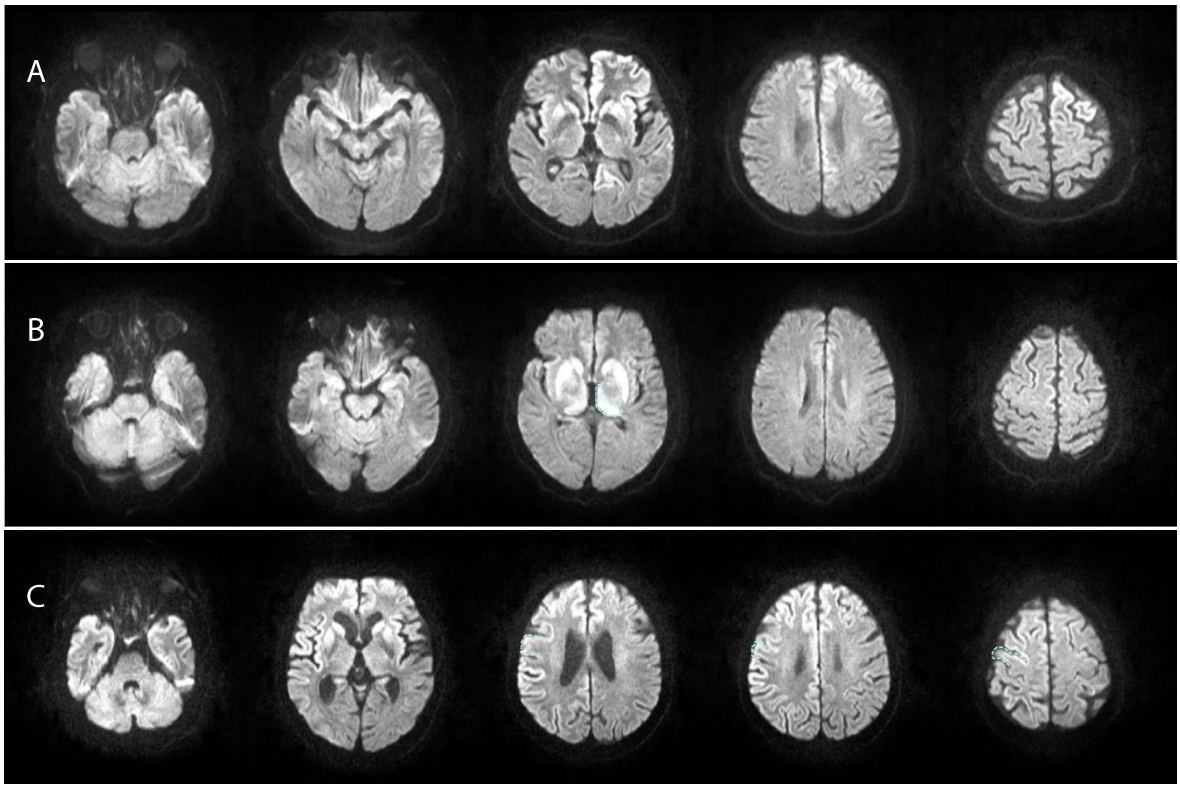

Figure 9. Lesion patterns of selected sJCD patients. **A** Typical distribution of sJCD lesions on DWI. One may notice the symmetric involvement of basal ganglia, temporal poles, frontal cortex and insular region. The motor cortex and cerebellum is spared. **B** Hockey stick sign in sJCD. The thalamic region is affected (highlighted area). **C** Involvement of motor cortex (right). High signal abnormalities of this patient's right motor cortex (highlighted area) was found in compliance to its left sided hemiparesis.

[13.2%]). 26.8% (SD, 26.8%) of sJCD were located in non-definable areas (ND) which could be assigned to cortices being connected through long-range fibres. The smallest amount of lesions were in cortices of the ILF (mean [SD] volume, 8.7% [9.6%]) and MdLF (mean [SD] volume, 9.2% [9.5%]). All results are displayed in figure 12. Notwithstanding, on average, 81.7% (SD, 26.8%) of sJCD lesions were located in association cortices (see Figure 13). It has to be mentioned that the overall share of association cortices in the AAL atlas compared to all other non-definable regions is only 32.5%.

3.4 Involvement of cortical systems in sJCD

After the assignment of areas the auditory, motor, somatosensory and visual system to the Talairach atlas in R, both sides of the brain were statistically examined and compared. Overall, the arithmetic mean of labelled sJCD lesions was 10804 mm^3 (SD, 4846 mm^3). No differences between all four systems of the left and right side of the brain could be shown (t [p-value] t-test, 0.67 [0.51]). Also the labelling revealed no significant differences in lesions affecting the auditory system (t [p-value] t-test, 0.82 [0.42]), the motor system (t [p-value] t-test, 0.51 [0.61]), the somatosensory system (t [p-value] t-test, 0.35 [0.73]) or the visual system (t [p-value] t-test, 0.22 [0.83]) between both sides of the cortex.

In Figure 14, the mean volumes of subsystems of the four abovementioned cortical systems are plotted. No system revealed to be significantly more or less affected by sJCD lesions compared to each other (chi^2 [p-value] Kruskal-Wallis test, 6.34 [0.09]). Otherwise, there are differences shown for the subsystems (chi^2 [p-value] Kruskal-Wallis test, 132.9 [<0.001]). The belt line is significantly more affected by lesions than the core areas in all four systems (p-value Wilcoxon rank test, <0.001), as well as the root areas, are less affected than a system's belt lines (p-value Wilcoxon rank test, <0.001). Between the core and root lines, no significant difference was revealed (p-value Wilcoxon rank test, 1.000). For the association cortices, paralimbic areas are stronger affected than prefrontal areas by sJCD lesions (p-value Wilcoxon rank test, <0.001). No significant differences could be shown between the multimodal cortices and the paralimbic regions (p-value Wilcoxon rank test, 0.08) or prefrontal areas (p-value Wilcoxon rank test, 0.10).

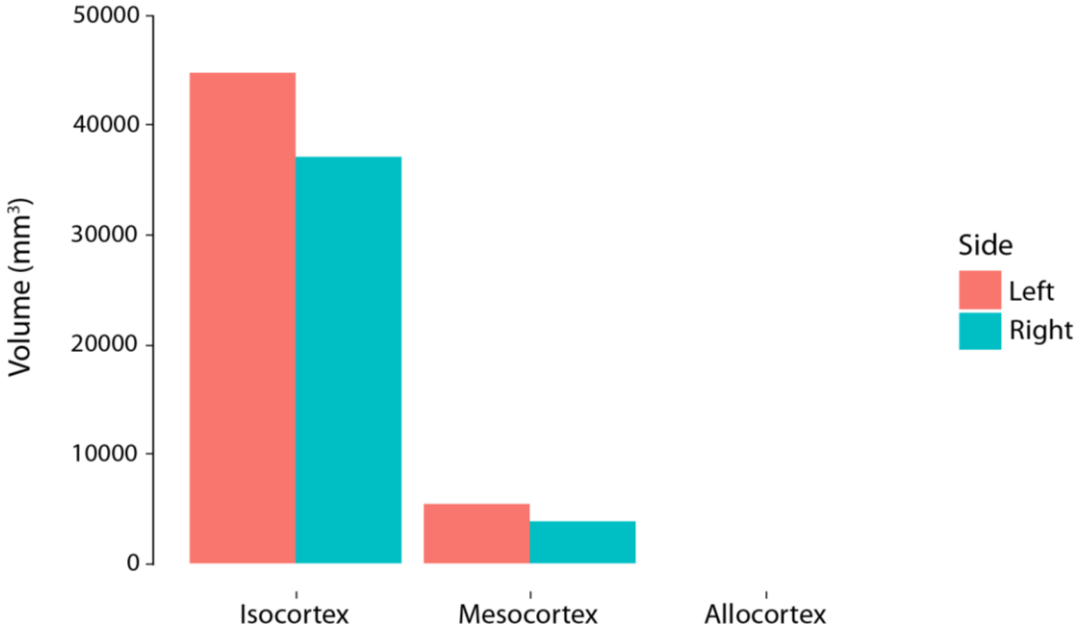

Figure 10. Volumes of phylogenetic cortices. The volumes are given in mm^2. One can observe that the major portion of lesions involve the isocortex. The volumes of lesions in the allocortex are so small that they do not appear in the bar plot.

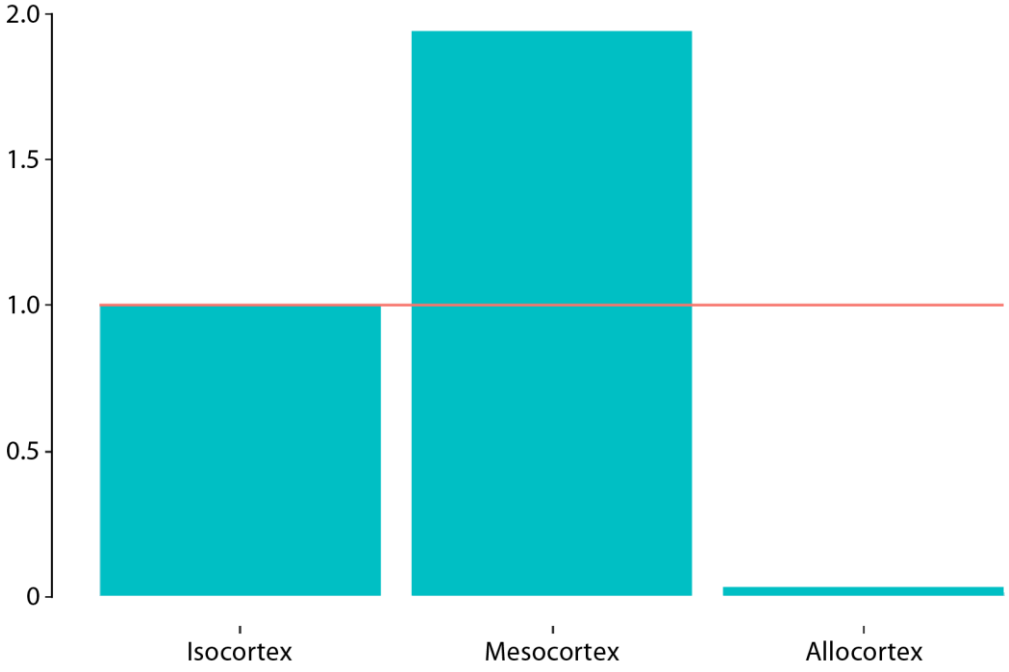

Figure 11. Ratio of Mesocortex and Allocortex to Isocortex (volume adjusted). The "homogeneity line" is illustrated in orange. The MRI lesions of sJCD subjects affect the mesocortex twice as often compared to the isocortex when considering the relative volumes of both cortices. The allocortex shows almost no involvement.

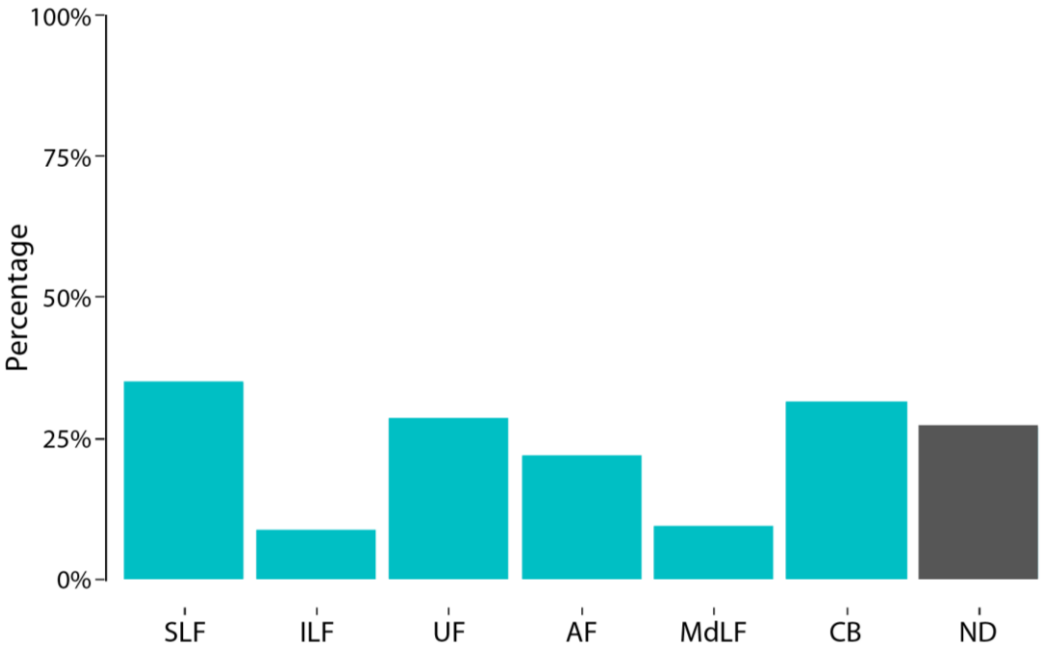

Figure 12. Percentages of sJCD lesions in areas of long-range fibre tracts. The tract volumes were assessed in relation to the whole volume of lesions. **SLF** – Superior longitudinal fasciculus; **ILF** – Inferior longitudinal fasciculus; **UF** – Uncinate fasciculus; **AF** – Arcuate fasciculus; **MdLF** – Middle longitudinal fasciculus; **CB** – Cingulate bundle; **ND** – Not definable areas

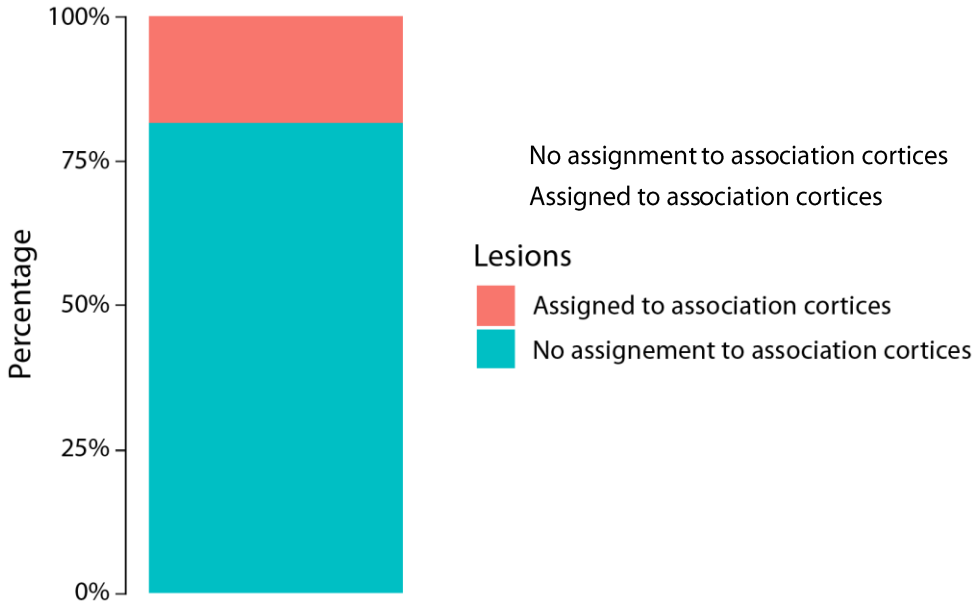

Figure 13. Percentage of sJCD lesions assigned to association cortices. The tract volumes were assessed in relation to the whole volume of lesions. **SLF** – Superior longitudinal fasciculus; **ILF** – Inferior longitudinal fasciculus; **UF** – Uncinate fasciculus; **AF** – Arcuate fasciculus; **MdLF** – Middle longitudinal fasciculus; **CB** – Cingulate bundle; **ND** – Not definable areas

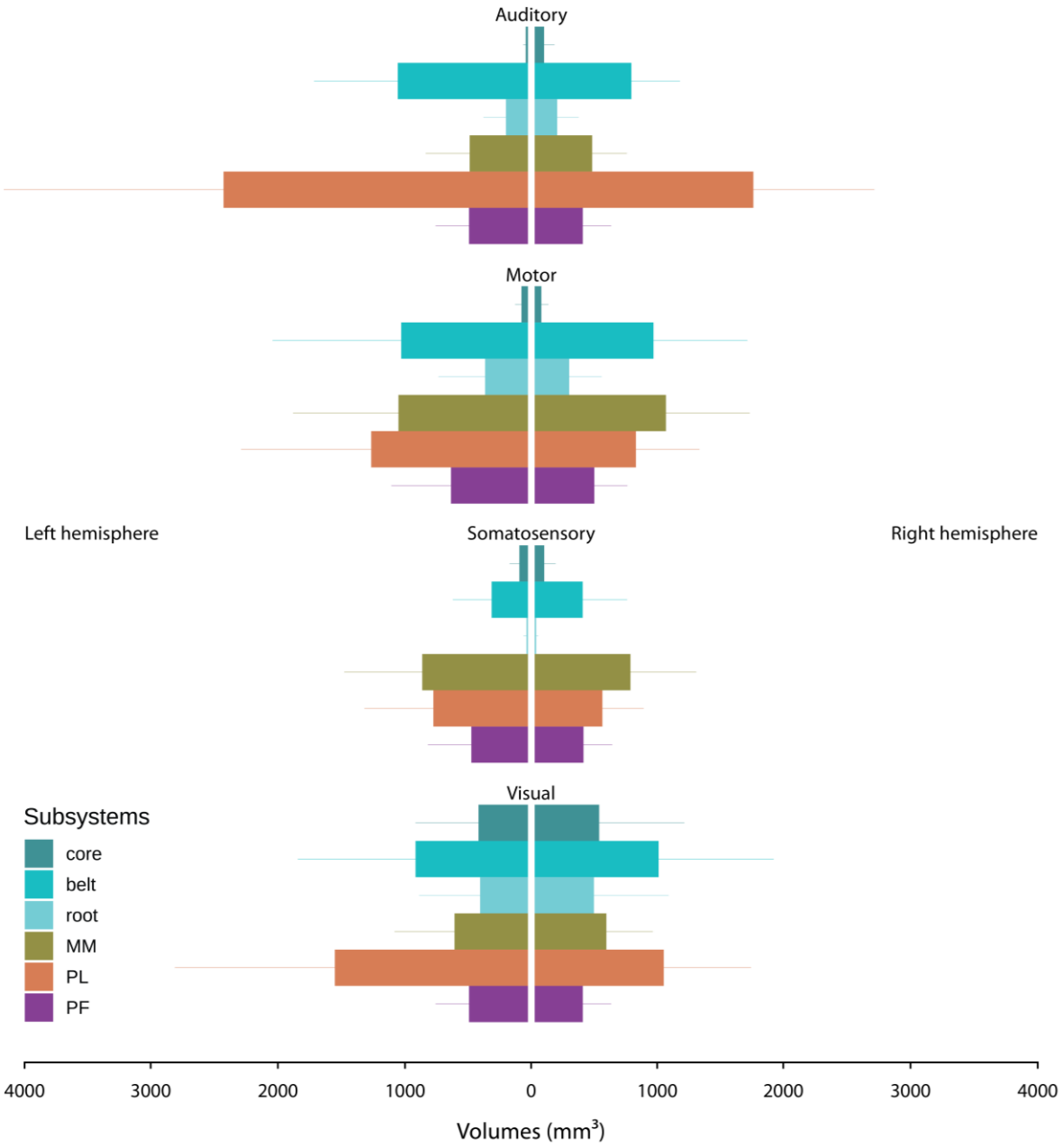

Figure 14. Volumes of sJCD lesions affecting cortical systems. Four systems which are subdivided into six subsystems are visualised based on their lesion patterns. One may notice that paralimbic areas (**PL**) and belt lines are predominantly often affected by sJCD lesions. Also the multimodal cortices (**MM**) are often involved. **PF** – prefrontal cortex.

Discussion

From the results of this thesis, one may conclude that most of the sJCD lesions are located in cortical areas of the isocortex. The mesocortex has a smaller volume compared to the isocortex but seems to be relatively more often involved. That is concordant with this thesis' other results showing a strong affection of paralimbic areas. This was expectable since other studies have shown similar DWI patterns (2,46,53,55). In contrast, DWI lesions seldom affected the allocortex, which could mean that the disease only happens in the evolutionary younger brain parts consisting of three to six neuronal layers. It has been shown, that PrP^{TSE} is produced primarily in the upper cortical layers II-IV and cerebellum (121), which might explain why sJCD shows diffusion restrictions, particularly in a patient's neocortex and mesocortex. Since the mesocortex is evolutionary localised between the neocortex and allocortex, its upper cortical layers II-IV are merged but existing, which is not the case in the allocortex. This factor might explain the numerous lesions found in the mesocortex but almost none in the allocortex.

This hypothesis is further supported by the typical symptoms patients have when suffering from sJCD. Rapidly progressive dementia plus further neurological symptoms like myocloni, pyramidal and extrapyramidal symptoms, ataxia or deterioration rather than an amnestic syndrome or changes in olfactory perception speak for the involvement of higher cortical areas but not the hippocampus or olfactory cortex. This „resistance of the hippocampus" has already been published by C. Masullo et al. (122) in 1997.

Interestingly, sJCD does not seem to occur predominantly in one side of an affected brain but at the same time has a strong connection to association cortices. This could mean that prions are in fact axonally transported between these association cortices but also over commissural fibres between both hemispheres. However, further studies with functional MRI imaging or tractography should be made to investigate this topic more thoroughly. By analysing the cortical lesion patterns alone, no definite conclusion about the involvement of distinct long-range white matter pathways can be drawn. Notwithstanding, particularly fibre tracts with associations mostly to the prefrontal, paralimbic or parietal cortices show DWI

alterations in this thesis's results. This is reasonable since these regions tend to show DWI abnormalities in most cases and are also supported by the cortical system and subsystem analysis (see Figure 14). On the other hand, some studies that consider only a little or no effect on disease progression by axonal PrP^{TSE} transport (123) and preferably a distribution of prions via glycosylphosphatidylinositol (GPI) anchored proteins in synaptic boutons or dendrites (124).

However, this thesis's results support the hypothesis of axonal transport of prions in sJCD to some degree with no assumption on the actual magnitude on disease progression or prion protein distribution in the brain. Further studies must be carried out on this topic.

There are some discrepancies in the connection between clinical manifestation of sJCD and the involvement of cortical systems. The involvement of the auditory cortex in the results does not comply with the patients symptomatic. No auditory disorders neither in the perception nor in the production of speech were found in the patients of this thesis but slurred speech in two patients which, however, was classified in both cases as dysarthria. Reduction of visual function was found in two patients which may reflect the lesion patterns in the results. Motor or somatosensory disorders were found in all patients with a substantial cerebellar or basal ganglia input concordant to the lesion patterns. Ergo, it should be assumed that the lesions patterns on MRI might correlate with patients neurological symptoms, as shown in former studies (2). However, sJCD shows a rapid reduction of multiple cortical functions and might not always show abnormalities on DWI or other sequences. Besides, different subtypes in sJCD express very different phenotypes which do not always correlate with a patient's MRI scan and sometimes aggravate the radiological diagnosis. Previous publication categorised these phenotypes in three variants calling them *Heidenhain*, *Brownell-Oppenheimer* and *Stern* (125–127) where, for instance, the Stern variant shows no DWI alterations, respectively the Brownell-Oppenheimer not in all cases. For that reason, MRI imaging continues to be an essential diagnostic tool in sJCD but will possibly not become the gold-standard for a definite diagnosis if there are no better sequences found or imaging patterns revealed.

The alleged sparing of the sensorimotor cortex (*Rolandic cortex*) being described in dozens of publications (2,46) and considered as atypical may be discussed as well. The results of this thesis revealed no difference between the motor system and all other systems. The core, root and belt lines were likewise involved by lesions with the belt lines being even affected the strongest on average compared to the other three systems. This is interesting since this region is directly located in the Rolandic cortex. In general, it appears to be counterintuitive for a disease with systemic aetiology and with patients showing symptoms of motor dysfunction to spare a neocortical region. It was shown that this phenomenon might occur due to an intrinsic feature of the Rolandic cortex appearing relatively hypointense to other neocortical areas on DWI but showing the same diffusion restrictions on ACD maps as well in sJCD (128). In this thesis, ADC maps were used simultaneously together with DWI scans for the labelling process showing lesions in area 1, 2 and 4 frequently. Therefore, the assumption that the Rolandic cortex is usually not affected by sJCD should be reconsidered.

Some limitations in this thesis have to be mentioned. The number of patients in this thesis was too low for a highly significant statistical analysis leading to high standard deviations. Therefore, further investigations with more patients should be made. There were not always post-mortem autopsy reports available, making a definite diagnosis for the whole cohort impossible. Since the quality and resolution in DWI is minor compared to other MRI sequences, but mandatory for diagnosing and evaluating JCD on imaging, the labelled regions' accuracy may be slightly reduced. Although the transformation of MNI coordinates to Talairach coordinates is accepted and frequently done, it underlies particular scaling and allocation biases and has to be mentioned. The underlying mathematical process and abovementioned biases are described by J. L. Lancaster (93). In respect of the method, it was impossible to distinguish precisely which lesions affect which subsystems or association tracts since their cortical locations overlap. As mentioned before, this thesis only examined DWI lesion patterns of the cortex and no white-matter imaging. Therefore, the relative or absolute results in this thesis have to be considered cautiously. Subsequently, only the most

conservative statistical methods and corrections were used in order to compensate for the abovementioned limitations, enabling the formulation of the hypotheses made in this discussion.

List of References

1. Centers for Disease Control and Prevention, CDC. (2018) Prion Diseases [Online]. Available at: https://www.cdc.gov/prions/index.html (Accessed: 26 May 2019).

2. Fragoso DC, Gonçalves Filho AL da M, Pacheco FT, Barros BR, Aguiar Littig I, Nunes RH, et al. Imaging of Creutzfeldt-Jakob Disease: Imaging Patterns and Their Differential Diagnosis. RadioGraphics. 2017 Jan;37(1):234–57.

3. Zerr I, Parchi P. Sporadic Creutzfeldt–Jakob disease. In: Handbook of Clinical Neurology [Internet]. Elsevier; 2018 [cited 2020 Jan 11]. p. 155–74. Available from: https://linkinghub.elsevier.com/retrieve/pii/B978044463945500009X

4. Ladogana A, Kovacs GG. Genetic Creutzfeldt–Jakob disease. In: Handbook of Clinical Neurology [Internet]. Elsevier; 2018 [cited 2020 Jan 11]. p. 219–42. Available from: https://linkinghub.elsevier.com/retrieve/pii/B9780444639455000131

5. Brandel J-P, Knight R. Variant Creutzfeldt–Jakob disease. In: Handbook of Clinical Neurology [Internet]. Elsevier; 2018 [cited 2020 Jan 11]. p. 191–205. Available from: https://linkinghub.elsevier.com/retrieve/pii/B9780444639455000118

6. Kobayashi A, Kitamoto T, Mizusawa H. Iatrogenic Creutzfeldt–Jakob disease. In: Handbook of Clinical Neurology [Internet]. Elsevier; 2018 [cited 2020 Jan 11]. p. 207–18. Available from: https://linkinghub.elsevier.com/retrieve/pii/B978044463945500012X

7. Takada LT, Kim M-O, Metcalf S, Gala II, Geschwind MD. Prion disease. In: Handbook of Clinical Neurology [Internet]. Elsevier; 2018 [cited 2020 Jan 11]. p. 441–64. Available from: https://linkinghub.elsevier.com/retrieve/pii/B9780444640765000296

8. Creutzfeldt HG. Über eine eigenartige herdförmige erkrankung des zentralnervensystems (Vorläufige mitteilung). Z Für Gesamte Neurol Psychiatr. 1920 Dec 1;57(1):1–18.

9. Triarhou LC. Alfons Maria Jakob (1884–1931), Neuropathologist par Excellence. Eur Neurol. 2009;61(1):52–8.

10. Jakob, A. D. Z.Nervenheilk. 70, 132-146 (1921a).

11. Jakob, A. Z.ges. Neurol. Psychiatr. 64, 147-228 (1921b).

12. Jakob, A. Med. Klin. 17, 382-386 (1921c).

13. Jakob A. Monogr. Gesamtgeb. Neurol. Psychiatr. 1923.

14. Wolf JH, Foley P. Hans Gerhard Creutzfeldt (1885–1964): a life in neuropathology. J Neural Transm. 2005 Aug;112(8):I–XCVII.

15. Manuelidis EE. J. Neuropathol. 1985.

16. Masters, C. L. & Gajdusek, D. C. in Recent advances in Neuropathology Vol. 2 (eds Smith, W. T. & Cavanagh, J. B.) 139-163 (Churchill Livingstone, Edinburgh, 1982).

17. Katscher F. It's Jakob's disease, not Creutzfeldt's. Nature. 1998 May 1;393(6680):11–11.

18. Gibbs CJ, Gajdusek DC, Asher DM, Alpers MP, Beck E, Daniel PM, et al. Creutzfeldt-Jakob Disease (Spongiform Encephalopathy): Transmission to the Chimpanzee. Science. 1968 Jul 26;161(3839):388.

19. Ladogana A, Puopolo M, Croes EA, Budka H, Jarius C, Collins S, et al. Mortality from Creutzfeldt–Jakob disease and related disorders in Europe, Australia, and Canada. Neurology. 2005 May 10;64(9):1586.

20. Richardson Jr EP, Masters CL. The Nosology of Creutzfeldt-Jakob Disease and Conditions Related to the Accumulation of PrPCJD in the Nervous System. Brain Pathol. 1995 Jan 1;5(1):33–41.

21. MASTERS c. L, RICHARDSON EP JR. SUBACUTE SPONGIFORM ENCEPHALOPATHY (CREUTZFELDT-JAKOB DISEASE): THE NATURE AND PROGRESSION OF SPONGIFORM CHANGE. Brain. 1978 Jun 1;101(2):333–44.

22. FIELD EJ, FARMER F, CASPARY EA, JOYCE G. Susceptibility of Scrapie Agent to Ionizing Radiation. Nature. 1969 Apr 1;222(5188):90–1.

23. Pattison IH. Resistance of the scrapie agent to formalin. J Comp Pathol. 1965 Apr 1;75(2):159–64.

24. Prusiner S. Novel proteinaceous infectious particles cause scrapie. Science. 1982 Apr 9;216(4542):136.

25. Prusiner SB. BIOLOGY AND GENETICS OF PRION DISEASES. Annu Rev Microbiol. 1994 Oct 1;48(1):655–86.

26. McAlister V. Sacred Disease of Our Times: Failure of the Infectious Disease Model of Spongiform Encephalopathy. Clin Invest Med. 2005;28(3):45.

27. GAJDUSEK DC, GIBBS CJ, ALPERS M. Experimental Transmission of a Kuru-like Syndrome to Chimpanzees. Nature. 1966 Feb 1;209(5025):794–6.

28. Gajdusek DC, Zigas V. Degenerative Disease of the Central Nervous System in New Guinea. N Engl J Med. 1957 Nov 14;257(20):974–8.

29. Collins S, Boyd A, Fletcher A, Gonzales MF, McLean CA, Masters CL. Recent advances in the pre-mortem diagnosis of Creutzfeldt-Jakob disease. J Clin Neurosci. 2000 May 1;7(3):195–202.

30. Geschwind MD. Prion Diseases. Contin Lifelong Learn Neurol [Internet]. 2015;21(6). Available from: https://journals.lww.com/continuum/Fulltext/2015/12000/Prion_Diseases.11.aspx

31. Masters CL, Harris JO, Gajdusek DC, Gibbs Jr CJ, Bernoulli C, Asher DM. Creutzfeldt-Jakob disease: Patterns of worldwide occurrence and the significance of familial and sporadic clustering. Ann Neurol. 1979 Feb 1;5(2):177–88.

32. Barnett F. Nursing patients with variant Creutzfeldt-Jakob disease at home. Br J Community Nurs. 2002 Sep 1;7(9):445–50.

33. Britton TC, Al-Sarraj S, Shaw C, Campbell T, Collinge J. Sporadic Creutzfeldt-Jakob disease in a 16-year-old in the UK. The Lancet. 1995 Oct 28;346(8983):1155.

34. Ritchie DL, Boyle A, McConnell I, Head MW, Ironside JW, Bruce ME. Transmissions of variant Creutzfeldt–Jakob disease from brain and lymphoreticular tissue show uniform and conserved bovine spongiform encephalopathy-related phenotypic properties on primary and secondary passage in wild-type mice. J Gen Virol. 2009;90(12):3075–82.

35. Urwin PJM, Mackenzie JM, Llewelyn CA, Will RG, Hewitt PE. Creutzfeldt–Jakob disease and blood transfusion: updated results of the UK Transfusion Medicine Epidemiology Review Study. Vox Sang. 2016 May 1;110(4):310–6.

36. Llewelyn C, Hewitt P, Knight R, Amar K, Cousens S, Mackenzie J, et al. Possible transmission of variant Creutzfeldt-Jakob disease by blood transfusion. The Lancet. 2004 Feb 7;363(9407):417–21.

37. Kovács GG, Puopolo M, Ladogana A, Pocchiari M, Budka H, van Duijn C, et al. Genetic prion disease: the EUROCJD experience. Hum Genet. 2005 Nov 1;118(2):166–74.

38. Parchi P, Giese A, Capellari S, Brown P, Schulz-Schaeffer W, Windl O, et al. classification of sporadic Creutzfeldt-Jakob disease based on molecular and phenotypic analysis of 300 subjects. Ann Neurol. 1999 Aug 1;46(2):224–33.

39. Parchi P, Capellari S, Chin S, Schwarz HB, Schecter NP, Butts JD, et al. A subtype of sporadic prion disease mimicking fatal familial insomnia. Neurology. 1999 Jun 1;52(9):1757.

40. Cracco L, Appleby BS, Gambetti P. Fatal familial insomnia and sporadic fatal insomnia. In: Handbook of Clinical Neurology [Internet]. Elsevier; 2018 [cited 2020 Jan 13]. p. 271–99. Available from: https://linkinghub.elsevier.com/retrieve/pii/B9780444639455000155

41. Parchi P, de Boni L, Saverioni D, Cohen ML, Ferrer I, Gambetti P, et al. Consensus classification of human prion disease histotypes allows reliable identification of molecular subtypes: an inter-rater study among surveillance centres in Europe and USA. Acta Neuropathol (Berl). 2012 Oct;124(4):517–29.

42. Manix M, Kalakoti P, Henry M, Thakur J, Menger R, Guthikonda B, et al. Creutzfeldt-Jakob disease: updated diagnostic criteria, treatment algorithm, and the utility of brain biopsy. Neurosurg Focus. 2015 Nov;39(5):E2.

43. Kim H-C, Chang K-H, Song IC, Lee SH, Kwon BJ, Han MH, et al. Diffusion-Weighted MR Imaging in Biopsy-Proven Creutzfeldt-Jakob Disease. Korean J Radiol. 2001;2(4):192.

44. Tschampa HJ, Kallenberg K, Urbach H, Meissner B, Nicolay C, Kretzschmar HA, et al. MRI in the diagnosis of sporadic Creutzfeldt–Jakob disease: a study on inter-observer agreement. Brain. 2005 Sep 1;128(9):2026–33.

45. Carswell C, Thompson A, Lukic A, Stevens J, Rudge P, Mead S, et al. MRI findings are often missed in the diagnosis of Creutzfeldt-Jakob disease. BMC Neurol. 2012 Dec;12(1):153.

46. Meissner B, Kallenberg K, Sanchez-Juan P, Collie D, Summers DM, Almonti S, et al. MRI lesion profiles in sporadic Creutzfeldt–Jakob disease. 2009;8.

47. Mendez OE, Shang J, Jungreis CA, Kaufer DI. Diffusion-Weighted MRI in Creutzfeldt-Jakob Disease: A Better Diagnostic Marker Than CSF Protein 14-3-3? J Neuroimaging. 2003 Apr;13(2):147–51.

48. Zerr I, Kallenberg K, Summers DM, Romero C, Taratuto A, Heinemann U, et al. Updated clinical diagnostic criteria for sporadic Creutzfeldt-Jakob disease. Brain. 2009 Oct 1;132(10):2659–68.

49. Diagnostic Criteria | Creutzfeldt-Jakob Disease, Classic (CJD) | Prion Disease | CDC [Internet]. 2019 [cited 2020 Jan 26]. Available from: https://www.cdc.gov/prions/cjd/diagnostic-criteria.html

50. Shiga Y, Miyazawa K, Sato S, Fukushima R, Shibuya S, Sato Y, et al. Diffusion-weighted MRI abnormalities as an early diagnostic marker for Creutzfeldt–Jakob disease. Neurology. 2004 Aug 10;63(3):443.

51. Collins SJ, Sanchez-Juan P, Masters CL, Klug GM, van Duijn C, Poleggi A, et al. Determinants of diagnostic investigation sensitivities across the clinical spectrum of sporadic Creutzfeldt–Jakob disease. Brain. 2006 Jul 1;129(9):2278–87.

52. Lodi R, Parchi P, Tonon C, Manners D, Capellari S, Strammiello R, et al. Magnetic resonance diagnostic markers in clinically sporadic prion disease: a combined brain

magnetic resonance imaging and spectroscopy study. Brain. 2009 Sep 15;132(10):2669–79.

53. Vitali P, Maccagnano E, Caverzasi E, Henry RG, Haman A, Torres-Chae C, et al. Diffusion-weighted MRI hyperintensity patterns differentiate CJD from other rapid dementias. Neurology. 2011 May 17;76(20):1711–9.

54. Meissner B, Köhler K, Körtner K, Bartl M, Jastrow U, Mollenhauer B, et al. Sporadic Creutzfeldt-Jakob disease. Neurology. 2004 Aug 10;63(3):450.

55. Bizzi A, Pascuzzo R, Blevins J, Grisoli M, Lodi R, Moscatelli MEM, et al. Evaluation of a New Criterion for Detecting Prion Disease With Diffusion Magnetic Resonance Imaging. JAMA Neurol [Internet]. 2020 Jun 1 [cited 2020 Aug 18]; Available from: https://jamanetwork.com/journals/jamaneurology/fullarticle/2766570

56. Manners DN, Parchi P, Tonon C, Capellari S, Strammiello R, Testa C, et al. Pathologic correlates of diffusion MRI changes in Creutzfeldt-Jakob disease. Neurology. 2009 Apr 21;72(16):1425.

57. Warden DR, Dennison JV, Limback J, Shroff SM, Messina SA. Imaging Manifestations of Creutzfeldt-Jakob Disease and Case Series. Cureus [Internet]. 2018 Dec 13 [cited 2019 May 27]; Available from: https://www.cureus.com/articles/12178-imaging-manifestations-of-creutzfeldt-jakob-disease-and-case-series

58. Collie DA, Summers DM, Sellar RJ, Ironside JW, Cooper S, Zeidler M, et al. Diagnosing Variant Creutzfeldt-Jakob Disease with the Pulvinar Sign: MR Imaging Findings in 86 Neuropathologically Confirmed Cases. Am J Neuroradiol. 2003 Sep 1;24(8):1560.

59. Bizzi A. Event-Based Model of Diffusion MRI Shows that sCJD Strains Have Similar Epicenter but Different Lesion Propagation in the Brain. In Chicago; 2018. Available from: http://archive.rsna.org/2018/18022933.pdf

60. Steinhoff BJ, Racker S, Herrendorf G, Poser S, Grosche S, Zerr I, et al. Accuracy and Reliability of Periodic Sharp Wave Complexes in Creutzfeldt-Jakob Disease. Arch Neurol. 1996 Feb 1;53(2):162–6.

61. Will RG. The spongiform encephalopathies. J Neurol Neurosurg Amp Psychiatry. 1991 Sep 1;54(9):761.

62. Haïk S, Brandel JP, Sazdovitch V, Delasnerie-Lauprêtre N, Peoc'h K, Laplanche J-L, et al. Dementia with Lewy bodies in a neuropathologic series of suspected Creutzfeldt–Jakob disease. Neurology. 2000 Nov 14;55(9):1401.

63. YEMISCI M, GURER G, SAYGI S, CIGER A. Generalised periodic epileptiform discharges: clinical features, neuroradiological evaluation and prognosis in 37 adult patients. Seizure. 2003 Oct 1;12(7):465–72.

64. Leitão MJ, Baldeiras I, Almeida MR, Ribeiro MH, Santos AC, Ribeiro M, et al. Sporadic Creutzfeldt–Jakob disease diagnostic accuracy is improved by a new CSF ELISA 14-3-3γ assay. Neuroscience. 2016 May 13;322:398–407.

65. Lattanzio F, Abu-Rumeileh S, Franceschini A, Kai H, Amore G, Poggiolini I, et al. Prion-specific and surrogate CSF biomarkers in Creutzfeldt-Jakob disease: diagnostic accuracy in relation to molecular subtypes and analysis of neuropathological correlates of p-tau and Aβ42 levels. Acta Neuropathol (Berl). 2017 Apr 1;133(4):559–78.

66. Rosenmann H, Meiner Z, Kahana E, Halimi M, Lenetsky E, Abramsky O, et al. Detection of 14-3-3 protein in the CSF of genetic Creutzfeldt-Jakob disease. Neurology. 1997 Aug 1;49(2):593.

67. Fourier A, Dorey A, Perret-Liaudet A, Quadrio I. Detection of CSF 14-3-3 Protein in Sporadic Creutzfeldt-Jakob Disease Patients Using a New Automated Capillary Western Assay. Mol Neurobiol. 2018 Apr 1;55(4):3537–45.

68. Varges D, Jung K, Gawinecka J, Heinemann U, Schmitz M, von Ahsen N, et al. Amyloid-β 1-42 Levels are Modified by Apolipoprotein E ε4 in Creutzfeldt-Jakob Disease in a Similar Manner as in Alzheimer's disease. J Alzheimers Dis. 2011 Mar 21;23(4):717–26.

69. Sanchez-Juan P, Green A, Ladogana A, Cuadrado-Corrales N, Sáanchez-Valle R, Mitrováa E, et al. CSF tests in the differential diagnosis of Creutzfeldt-Jakob disease. Neurology. 2006 Aug 22;67(4):637.

70. Forner SA, Takada LT, Bettcher BM, Lobach IV, Tartaglia MC, Torres-Chae C, et al. Comparing CSF biomarkers and brain MRI in the diagnosis of sporadic Creutzfeldt-Jakob disease. Neurol Clin Pract. 2015 Apr 1;5(2):116.

71. Kasai T, Tokuda T, Ishii R, Ishigami N, Tsuboi Y, Nakagawa M, et al. Increased α-synuclein levels in the cerebrospinal fluid of patients with Creutzfeldt–Jakob disease. J Neurol. 2014 Jun 1;261(6):1203–9.

72. Llorens F, Kruse N, Schmitz M, Gotzmann N, Golanska E, Thüne K, et al. Evaluation of α-synuclein as a novel cerebrospinal fluid biomarker in different forms of prion diseases. Alzheimers Dement. 2017 Jun 1;13(6):710–9.

73. Atarashi R, Sano K, Satoh K, Nishida N. Real-time quaking-induced conversion: a highly sensitive assay for prion detection. Prion. 2011;5(3):150–3.

74. Atarashi R, Satoh K, Sano K, Fuse T, Yamaguchi N, Ishibashi D, et al. Ultrasensitive human prion detection in cerebrospinal fluid by real-time quaking-induced conversion. Nat Med. 2011 Feb 1;17(2):175–8.

75. Cramm M, Schmitz M, Karch A, Zafar S, Varges D, Mitrova E, et al. Characteristic CSF Prion Seeding Efficiency in Humans with Prion Diseases. Mol Neurobiol. 2015 Feb 1;51(1):396–405.

76. Bongianni M, Orrù C, Groveman BR, Sacchetto L, Fiorini M, Tonoli G, et al. Diagnosis of Human Prion Disease Using Real-Time Quaking-Induced Conversion Testing of Olfactory Mucosa and Cerebrospinal Fluid Samples. JAMA Neurol. 2017 Feb 1;74(2):155–62.

77. Orrú CD, Groveman BR, Hughson AG, Zanusso G, Coulthart MB, Caughey B. Rapid and Sensitive RT-QuIC Detection of Human Creutzfeldt-Jakob Disease Using Cerebrospinal Fluid. Wickner RB, editor. mBio. 2015 Feb 27;6(1):e02451-14.

78. Damadian R. Tumor Detection by Nuclear Magnetic Resonance. Science. 1971 Mar 19;171(3976):1151.

79. Chang K. Denied Nobel for M.R.I., He Wins Another Prize. The New York Times [Internet]. 2004 Mar 23 [cited 2020 Jan 27]; Available from: https://www.nytimes.com/2004/03/23/science/denied-nobel-for-mri-he-wins-another-prize.html

80. Schmidt-Böcking H, Schmidt L, Lüdde HJ, Trageser W, Templeton A, Sauer T. The Stern-Gerlach experiment revisited. Eur Phys J H. 2016 Nov 1;41(4):327–64.

81. Rabi II, Zacharias JR, Millman S, Kusch P. A New Method of Measuring Nuclear Magnetic Moment. Phys Rev. 1938 Feb 15;53(4):318–318.

82. Purcell EM, Torrey HC, Pound RV. Resonance Absorption by Nuclear Magnetic Moments in a Solid. Phys Rev. 1946 Jan 1;69(1–2):37–8.

83. Bloch F, Hansen WW, Packard M. The Nuclear Induction Experiment. Phys Rev. 1946 Oct 1;70(7–8):474–85.

84. Bloembergen N. Nonlinear Optics [Internet]. WORLD SCIENTIFIC; 1996 [cited 2020 Aug 19]. 188 p. Available from: https://doi.org/10.1142/3046

85. Lauterbur PC. Image Formation by Induced Local Interactions: Examples Employing Nuclear Magnetic Resonance. Nature. 1973 Jan 3;242.

86. Mansfield P, Maudsley AA. Medical imaging by NMR. Br J Radiol. 1977 Mar;50(591):188–94.

87. The Nobel Prize in Physiology or Medicine 2003 [Internet]. NobelPrize.org. [cited 2020 Aug 19]. Available from: https://www.nobelprize.org/prizes/medicine/2003/summary/

88. The Nobel Prize in Chemistry 1991 [Internet]. NobelPrize.org. [cited 2020 Aug 19]. Available from: https://www.nobelprize.org/prizes/chemistry/1991/summary/

89. Gertz H-J, Henkes N, Cervos-Navarro J. Creutzfeldt-Jakob disease. Neurology. 1988 Sep 1;38(9):1481.

90. Geschwind MD, Potter CA, Sattavat M, Garcia A, Rosen HJ, Miller BL, et al. Correlating DWI MRI with pathological and other features of Jakob-Creutzfeldt disease. 2010;13.

91. Brodmann K. Vergleichende Lokalisationslehre der Grosshirnrinde in ihren Prinzipien dargestellt auf Grund des Zellenbaues [Internet]. Leipzig : Barth; 1909 [cited 2020 Aug 30]. 346 p. Available from: http://archive.org/details/b28062449

92. Talairach J, Tournoux P. Co-planar Stereotaxic Atlas of the Human Brain: 3-Dimensional Proportional System - an Approach to Cerebral Imaging. New York: Thieme Medical Publisher; 1988.

93. Lancaster JL, Tordesillas-Gutiérrez D, Martinez M, Salinas F, Evans A, Zilles K, et al. Bias between MNI and Talairach coordinates analysed using the ICBM-152 brain template. Hum Brain Mapp. 2007 Nov;28(11):1194–205.

94. Brett M, Christoff K, Cusack R, Lancaster J. Using Talairach atlas with the MNI template. Neuroimage. 2001 Jun 1;13:85–85.

95. Strominger NL, Demarest RJ, Laemle LB. Cerebral Cortex. In: Strominger NL, Demarest RJ, Laemle LB, editors. Noback's Human Nervous System, Seventh Edition: Structure and Function [Internet]. Totowa, NJ: Humana Press; 2012. p. 429–51. Available from: https://doi.org/10.1007/978-1-61779-779-8_25

96. Makris N, Kaiser J, Haselgrove C, Seidman LJ, Biederman J, Boriel D, et al. Human cerebral cortex: A system for the integration of volume- and surface-based representations. NeuroImage. 2006 Oct;33(1):139–53.

97. Rolls ET, Joliot M, Tzourio-Mazoyer N. Implementation of a new parcellation of the orbitofrontal cortex in the automated anatomical labeling atlas. NeuroImage. 2015 Nov;122:1–5.

98. Hua K, Oishi K, Zhang J, Wakana S, Yoshioka T, Zhang W, et al. Mapping of Functional Areas in the Human Cortex Based on Connectivity through Association Fibers. :7.

99. JONES EG, POWELL TPS. AN ANATOMICAL STUDY OF CONVERGING SENSORY PATHWAYS WITHIN THE CEREBRAL CORTEX OF THE MONKEY. Brain. 1970 Jan 1;93(4):793–820.

100. Connectome - Homepage [Internet]. [cited 2020 Sep 13]. Available from: https://www.humanconnectome.org/

101. Swanson LW, Hahn JD, Sporns O. Organizing principles for the cerebral cortex network of commissural and association connections. Proc Natl Acad Sci. 2017 Nov 7;114(45):E9692–701.

102. Pandya D, Seltzer B, Petrides M, Cipolloni PB. Cerebral CortexArchitecture, Connections, and the Dual Origin Concept: Architecture, Connections, and the Dual Origin Concept [Internet]. Oxford, UK: Oxford University Press; 2015. Available from: https://oxfordmedicine.com/view/10.1093/med/9780195385151.001.0001/med-9780195385151

103. Wakana S, Jiang H, Nagae-Poetscher LM, van Zijl PCM, Mori S. Fiber Tract–based Atlas of Human White Matter Anatomy. Radiology. 2004 Jan 1;230(1):77–87.

104. Schmahmann JD, Pandya DN, Wang R, Dai G, D'Arceuil HE, de Crespigny AJ, et al. Association fibre pathways of the brain: parallel observations from diffusion spectrum imaging and autoradiography. Brain. 2007 Mar 1;130(3):630–53.

105. Martino J, Brogna C, Robles SG, Vergani F, Duffau H. Anatomic dissection of the inferior fronto-occipital fasciculus revisited in the lights of brain stimulation data☆. Cortex. 2010 May;46(5):691–9.

106. Bouzamondo-Bernstein E, Hopkins SD, Spilman P, Uyehara-Lock J, Deering C, Safar J, et al. The Neurodegeneration Sequence in Prion Diseases: Evidence from Functional, Morphological and Ultrastructural Studies of the GABAergic System. J Neuropathol Exp Neurol. 2004 Aug;63(8):882–99.

107. Caverzasi E, Mandelli ML, DeArmond SJ, Hess CP, Vitali P, Papinutto N, et al. White matter involvement in sporadic Creutzfeldt-Jakob disease. Brain. 2014 Dec;137(12):3339–54.

108. Lee H, Cohen OS, Rosenmann H, Hoffmann C, Kingsley PB, Korczyn AD, et al. Cerebral White Matter Disruption in Creutzfeldt-Jakob Disease. Am J Neuroradiol. 2012 Nov 1;33(10):1945.

109. Kalyvas A, Koutsarnakis C, Komaitis S, Karavasilis E, Christidi F, Skandalakis GP, et al. Mapping the human middle longitudinal fasciculus through a focused anatomo-imaging study: shifting the paradigm of its segmentation and connectivity pattern. Brain Struct Funct. 2020 Jan;225(1):85–119.

110. Caspers S, Geyer S, Schleicher A, Mohlberg H, Amunts K, Zilles K. The human inferior parietal cortex: Cytoarchitectonic parcellation and interindividual variability. NeuroImage. 2006 Nov;33(2):430–48.

111. Zilles K, Amunts K. Centenary of Brodmann's map — conception and fate. Nat Rev Neurosci. 2010 Feb;11(2):139–45.

112. Munoz-Lopez MM, Mohedano-Moriano A, Insausti R. Anatomical Pathways for Auditory Memory in Primates. Front Neuroanat [Internet]. 2010 [cited 2020 Sep 20];4. Available from: http://journal.frontiersin.org/article/10.3389/fnana.2010.00129/abstract

113. Morosan P, Rademacher J, Schleicher A, Amunts K, Schormann T, Zilles K. Human Primary Auditory Cortex: Cytoarchitectonic Subdivisions and Mapping into a Spatial Reference System. NeuroImage. 2001 Apr;13(4):684–701.

114. Scheperjans F, Eickhoff SB, Homke L, Mohlberg H, Hermann K, Amunts K, et al. Probabilistic Maps, Morphometry, and Variability of Cytoarchitectonic Areas in the Human Superior Parietal Cortex. Cereb Cortex. 2008 Sep 1;18(9):2141–57.

115. SPM12 - Statistical Parametric Mapping [Internet]. [cited 2020 Jan 10]. Available from: https://www.fil.ion.ucl.ac.uk/spm/software/spm12/

116. MATLAB - MathWorks [Internet]. [cited 2020 Sep 23]. Available from: https://de.mathworks.com/products/matlab.html

117. NITRC: MRIcroGL: Tool/Resource Info [Internet]. [cited 2020 Sep 23]. Available from: https://www.nitrc.org/projects/mricrogl

118. Yun-Shiuan C. yunshiuan/label4MRI [Internet]. 2020 [cited 2020 Sep 24]. Available from: https://github.com/yunshiuan/label4MRI

119. RStudio | Open source & professional software for data science teams - RStudio [Internet]. [cited 2020 Sep 24]. Available from: https://rstudio.com/

120. NITRC: MRIcron: Tool/Resource Info [Internet]. [cited 2020 Sep 24]. Available from: https://www.nitrc.org/projects/mricron

121. Jansen GH, Vogelaar CF, Elshof SM. Distribution of Cellular Prion Protein in Normal Human Cerebral Cortex – Does It Have Relevance to Creutzfeldt-Jakob Disease? Clin Chem Lab Med [Internet]. 2001 Jan 25 [cited 2020 Dec 31];39(4). Available from: https://www.degruyter.com/doi/10.1515/CCLM.2001.045

122. Masullo C, Macćhi G. Resistance of the hippocampus in Creutzfeldt-Jakob disease. Clin Neuropathol. 1997;16 1:37–44.

123. Rodolfo K, Hässig R, Moya KL, Frobert Y, Grassi J, Giamberardino LD. A novel cellular prion protein isoform present in rapid anterograde axonal transport. NeuroReport [Internet]. 1999;10(17). Available from: https://journals.lww.com/neuroreport/Fulltext/1999/11260/A_novel_cellular_prion_protein_isoform_present_in.32.aspx

124. Kooyman DL, Byrne GW, Logan JS. Glycosyl Phosphatidylinositol Anchor. Nephron Exp Nephrol. 1998;6(2):148–51.

125. Baiardi S, Capellari S, Ladogana A, Strumia S, Santangelo M, Pocchiari M, et al. Revisiting the Heidenhain Variant of Creutzfeldt-Jakob Disease: Evidence for Prion Type Variability Influencing Clinical Course and Laboratory Findings. J Alzheimers Dis. 2016;50(2):465–76.

126. Brownell B, Oppenheimer DR. An ataxic form of subacute presenile polioencephalopathy (Creutzfeldt-Jakob disease). J Neurol Neurosurg Amp Psychiatry. 1965 Aug 1;28(4):350.

127. STERN K. SEVERE DEMENTIA ASSOCIATED WITH BILATERAL SYMMETRICAL DEGENERATION OF THE THALAMUS1. Brain. 1939 Jun 1;62(2):157–71.

128. Lin Y-R, Young GS, Chen N-K, Dillon WP, Wong S. Creutzfeldt-Jakob Disease Involvement of Rolandic Cortex: A Quantitative Apparent Diffusion Coefficient Evaluation. Am J Neuroradiol. 2006 Sep 1;27(8):1755.

Appendix

All R scripts are available in the author's GitHub repository: [Link to repository]

R Script "Label4MRI"

```r
library("devtools")
library(label4MRI)
library(dplyr)

#Get data
m <- read.csv(".csv") #insert scan or patient ID

#Assign areas
Results <- t(mapply(
  FUN = mni_to_region_name, x = m$x, y = m$y, z = m$z, template = c("aal", "ba")))
write.csv(Results,".csv")


```

Example of assignments of AAL areas to phylogenetic cortices

```r
#Assign to phylogenetic areas
Meso <- filter(m, aal.label %in% c(
  "Cingulum_Ant_L",
  "Cingulum_Ant_R",
  "Cingulum_Mid_L",
  "Cingulum_Mid_R",
  "Cingulum_Post_L",
  "Cingulum_Post_R",
  "ParaHippocampal_L",
  "ParaHippocampal_R"
)
      )
Meso <- sum(Meso$n)

```

Code for plotting of lesions involving cortical systems (see Figure 14)

```r
#Bar plot absolute
n <- read.csv("Right Systems.csv") # or "Left Systems.csv"
#reorder
n$Subsystem <- factor(n$Subsystem, levels=c("core", "belt", "root", "MM", "PL", "PF"))

pp <- ggplot(data=n, aes(fill = Subsystem, x = System, y = Volumes_avg)) +
  geom_bar(stat="identity", position= "dodge") +
  geom_errorbar(aes(ymin=Volumes_avg, ymax=Volumes_avg+SD, color=factor(Subsystem)),
                size=.1,
                width=0,                    # Width of the error bars
                position=position_dodge(.9)) +
  scale_color_manual("Subsystems", values=c(
    "#3d9093","#00bfc4","#66d9dc","#938e46","#d87c54","#853d93"))+
  scale_fill_manual("Subsystems", values= c(
    "core" = "#3d9093", "belt" = "#00bfc4", "root" = "#66d9dc", "MM"="#938e46", "PL"="#d87c54", "PF"="#853d93"))+
  theme_tufte(base_size=13,  base_family="Myriad Pro")+
  ylim(0, 4500)
pp

```

Example – Statistics and results of phylogenetic ratios (see Figure 11)

```
#Student's t-test and mean (SD)
adx <- 1
ady <- 2
x <- c(r$Vol_1[adx], r$Vol_2[adx], r$Vol_3[adx], r$Vol_4[adx], r$Vol_5[adx],r$Vol_6[adx]
y <- c(r$Vol_1[ady], r$Vol_2[ady], r$Vol_3[ady], r$Vol_4[ady], r$Vol_5[ady],r$Vol_6[ady]
t.test(x, y)
b <- x+y
sd(b)
mean(b)

#Consider percentage of Allocortex/Mesocortex
m2 <- read.csv("Auswertung.csv")
Iso <- m2$Volume_total[1:2]
Iso <- sum(Iso)
Meso <- (m2$Volume_total[3:4])
Meso <- sum(Meso)*17
Allo <- (m2$Volume_total[5:6])
Allo <- sum(Allo)*8.5
Meso <- Meso/Iso
Allo <- Allo/Iso
Iso <- Iso/Iso

rat <- data.frame(
  Phylogenetic = c("Isocortex", "Mesocortex", "Allocortex"),
  Volume = c(Iso, Meso, Allo)
    )

iso2 <- m2$Volume_total2[1:20]
meso2 <- (m2$Volume_total2[21:40])*17
meso2 <- meso2/iso2
allo2 <- (m2$Volume_total2[41:60])*8.5
allo2 <- allo2/iso2
mean(allo2)
sd(allo2)
```

Example of assignments of Brodmann areas to long-range fibres

```
library(dplyr)
library(ggplot2)
library(ggthemes)
library(extrafont)
library(showtext)
library(devtools)
showtext_auto()

#Assign Brodmann to tracts
m <- read.csv("Tracts.csv")
data <- filter(m, ba.distance == 0)
x <- table(data$ba.label)
co <- data %>% count(ba.label)

SLF <- filter(co, ba.label %in% c(
  "Left-BA31",
  "Left-BA39",
  "Left-BA40",
  "Left-BA44",
  "Left-BA46",
  "Left-BA6",
  "Left-BA7",
  "Left-BA8",
  "Left-BA9",
  "Left-SensoryAssoc (5)",
  "Right-BA31",
  "Right-BA39",
  "Right-BA40",
  "Right-BA44",
  "Right-BA46",
  "Right-BA6",
  "Right-BA7",
  "Right-BA8",
  "Right-BA9",
  "Right-SensoryAssoc (5)"
)
)
```